Supporting Information for

Heteroatom Manipulation of Zeolite Crystallization: Stabilizing Zn-FAU against Interzeolite Transformation

Adam J. Mallette[1], Sungil Hong[2], Emily E. Freeman[2], Sarah A. Saslow[3], Sebastian Mergelsberg[3], Radha K. Motkuri[3], James J. Neeway[3], Giannis Mpourmpakis[2,]*, Jeffrey D. Rimer[1,]*

[1]Department of Chemical and Biomolecular Engineering, University of Houston, Houston, TX 77204, USA

[2]Department of Chemical and Petroleum Engineering, University of Pittsburgh, Pittsburgh, PA 15213, USA

[3]Pacific Northwest National Laboratory, Energy and Environment Directorate, Richland, WA 99354, USA

*Correspondence sent to: gmpourmp@pitt.edu and jrimer@central.uh.edu

Table of Contents

List of Figures and Tables

Figure S1: Time-resolved X-ray diffraction (XRD) patterns of the FAU-to-GIS interzeolite transformation

Figure S2: Scanning electron micrographs of the FAU-to-GIS interzeolite transformation

Figure S3: XRD patterns for zeolite syntheses in the presence of various multivalent species

Figure S4: XRD patterns illustrating the effect of different zinc sources

Figure S5: XRD patterns illustrating a phase shift from FAU towards LTA in the presence of Zn

Figure S6: XRD patterns illustrating the effect of the Zn/Al molar ratio on product phase outcomes

Figure S7: XRD patterns illustrating the effect of intermediate zinc addition on product phase outcomes

Figure S8: ICP analysis of supernatant composition throughout Zn,Na-FAU synthesis

Figure S9: Time-resolved elemental analysis of supernatant composition in the absence and presence of Zn

Figure S10: Characterization of as-synthesized VPI-7 (VSV type)

Figure S11: Oligomeric structures investigated in computational studies

Figure S12: Gibbs free energy profiles of (metallo-)silicate oligomerization

Figure S13: Dimerization energetics and optimized transition state structures of (metallo-)silicates

Figure S14: EXAFS analysis fits of Zn,Na-FAU products

Figure S15: Effects of dilution on physicochemical and visual properties of solid and supernatant phases

Figure S16: PDF measurements and analysis of Zn,Na-FAU products

Figure S17: ONIOM calculation schemes of FAU and GIS frameworks

Figure S18: Electronic energies of Al- and Zn- substitution into FAU and GIS frameworks

Supporting Methods

EXAFS and PDF analysis

Extended x-ray adsorption fine structure (EXAFS) measurements were collected at APS beamline 20-BM using a Si(III) double-crystal monochromator to select the incident energy and 50:50 He:N_2 and N_2 filled ion chambers to monitor the flux. The monochromator was calibrated using Zn foil (9.659 keV) for collecting Zn K edge EXAFS spectra. EXAFS spectra were collected in transmission mode. The pre-edge region was collected from 150 eV to 20 eV below the edge with a step size of 5 eV and a collection time of 0.51 sec at each step. From 20 eV below the edge to 40 eV above the edge, data was collected in 0.40 eV steps for 0.51 sec at each step. Post-edge data was collected to 16 k and obtained with a 0.05 k step size with a k weight of 0.4 and a collection time of 0.51 sec. Samples were pressed as 13 mm diameter pellets. The total mass of the samples was approximately 30 - 50 mg. EXAFS spectra were collected in duplicate or triplicate sets with the Zn foil as an inline reference.

Total X-ray scattering for Pair Distribution Function (PDF) analysis was measured at BL 11-ID-B of the APS using the 2D amorphous-Si PerkinElmer detector (2048 × 2048 pixels, 200 × 200 μm^2 pixel size)[2]. Structure and mineral composition of all precipitates were determined at a X-ray beam energy of 58.6 keV (λ = 0.2115 Å). All samples were mounted in 1.1 mm ID polyimide (Kapton) capillaries and measured at a distance of 160 mm. NIST CeO_2 diffraction standard set 674a; 1:20 dilution with glassy carbon was used to calibrate the sample-to-detector distance, tilt, and pitch of the detector. Threshold, spot, and polygon masks were applied to the data to remove (1) the beam stop (polygon mask) and (2) over/underexposed pixels (threshold and spot masks). 2D scattering data was integrated from q = 0.6 to 24.0 $Å^{-1}$ in GSAS-II using a 0.99 polarization correction to produce 1D profiles[3]. PDF profiles were calculated in PDFgetX3[4], using an empty capillary as the background reference.

EXAFS data normalization and energy calibration was performed using ATHENA software[5]. Zn EXAFS spectra were energy calibrated using the Zn foil reference spectrum collected simultaneously with the sample spectrum. Processed EXAFS spectra were fit using a shell-by-shell approach in ARTEMIS software. Model CIFs for hemimorphite[6] and a Zn-Faujasite framework (generated in VASP[7] and converted to CIF using Ovito (v. 3.5) and Vesta (v. 3)) were used to fit the sample spectra.

First-principles calculations

Density functional theory (DFT) calculations were performed using the Gaussian 09 software package[8] to investigate the initial oligomerization/cyclization thermodynamics of small zeolite precursor species. The global hybrid Minnesota functional with a high percentage of Hartree-Fock exchange (M062X) was used as it accurately describes main-group chemistry[9] with Pople's split-valence triple-zeta basis set with polarizable functions (6-311G(d,p)). Frequency calculations were performed after full optimizations to verify that the obtained structures were minima of the potential energy surface. To account for the hydrothermal environment in the pre-nucleation stage, the conductor-like polarizable continuum model (CPCM)[10] was applied using water as a solvent. In addition, the Gibbs free energy of reactions was calculated by applying thermochemistry including enthalpic and entropic corrections to the electronic energy at elevated temperature (373 K, similar to experiments). The growth process of oligomers is assumed to occur via (1) monomer addition, (2) condensation, and (3) water removal. Cyclic species are assumed to form by intramolecular condensation (i.e., cyclization) of linear species[11], followed by release of water to the liquid phase. A 3-membered ring is produced by cyclization of a linear trimer and tetramer cyclization results in a (3-1)-ring or a 4-membered ring. Full pathways including monomer addition, condensation, cyclization reaction, and water removal steps are found in Figure S12. For aluminosilicate and zincosilicate systems, no more than one aluminate ($Al(OH)_3(H_2O)$) or zincate monomer ($Zn(OH)_2(H_2O)_2$) is considered, which is added to a silicate monomer ($Si(OH)_4$) at the first addition step. All possible positions of aluminum and zinc were examined on the complexes larger than dimer, and the formation energies of the most stable

species are reported. A pH neutral environment is assumed to maintain a charge neutral growth system which does not require charge balancing counter-ions and explicit solvent molecules to provide charge stabilization. Although this may not represent a typical experimental setting for zeolite synthesis, it is proven to be an effective approach to obtain general trends of aluminosilicate species growth while maintaining reasonable computational cost[12].

The incorporation of aluminum and zinc into FAU and GIS zeolite frameworks were investigated by the ONIOM scheme[13] as implemented in Gaussian 09 software. The ONIOM method accurately describes chemistry on zeolite frameworks that are otherwise computationally infeasible to be calculated solely with ab-initio methods due to the materials' large size[14, 15]. FAU and GIS crystalline structures were obtained from the International Zeolite Association (IZA) and appropriate systems representing the relevant framework while maintaining a viable computation cost were constructed. All marginal oxygen atoms are terminated with hydrogens to maintain a neutral charge. The FAU and GIS structures contain 426 and 480 atoms, respectively, including the terminal hydrogens. Each structure was divided into two layers that were treated with different computational methods: high-level theory layer with M062X/6-311G(d,p), and low-level theory layer with the semi-empirical PM6 method[16]. Two tetrahedral sites that are crystallographically identical but differ in their relative location to the whole structure (one at the surface and the other in the bulk) were assigned to the high ONIOM layer along with the surrounding atoms. All remaining atoms belong to the low layer. This calculation scheme allowed for a direct comparison of the Al/Zn substitution energy at different locations (surface vs. bulk) on two frameworks (FAU vs. GIS). Since the number of atoms in the high layer (DFT) strongly affects the accuracy and cost of calculation, we carried out calculations with three different sizes of the high layer (see Figure S17). Benchmark results are described below (Figure S18) and energy values determined with the large partitioning scheme are reported in the manuscript (Figure 7). Since it was found that full relaxation of atoms in the low layer does not lead to significant deviations from their crystallographic positions, we did not freeze any atoms during optimizations. When one silicon atom is replaced by zinc, two protons are added to neighboring oxygen atoms to compensate the negative charges that stem from placing a divalent metal (Zn^{2+}) in a tetrahedral coordination. Similarly, one proton is added for aluminum substitution. As the initial position of the additional proton affects the substitution energy, we produced 15 different initial structures by randomly placing H atoms on first neighbor oxygen bridges, reporting the most negative values.
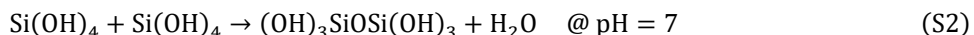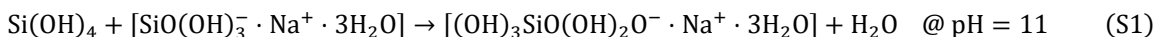
1. *Detailed formation energetics of oligomers*
Oligomerization pathways of pure-silicate, aluminosilicate (containing 1 Al), and zincosilicate (containing 1 Zn) species are calculated by DFT (see Figure S12). Optimized molecular structures are shown in Figure S11. Growth of linear species (monomer (M) → dimer (D) → trimer (Tr) → tetramer (T)) is assumed to occur via (1) addition of a monomeric species, (2) a condensation reaction, and (3) water removal. Cyclic structures are produced by an intramolecular reaction (i.e., ring-closure reaction) on linear trimers (to 3-membered ring (3R)) and tetramers (to 3-membered ring with one acyclic silicon, (3-1)R, or 4-membered ring (4R)), followed by water removal. The monomer addition steps in the pure-silicate system ("+Si" in Figure S12, black) are consistently endothermic ($\geq$ 7 kJ/mol). However, all the condensation/cyclization steps and water desorption steps are exothermic (except for the thermoneutral cyclization of Tr → 3R), which leads to the overall downhill energy landscape. The oligomerization energetics of the aluminosilicate (Figure S12, red) and zincosilicate (Figure S12, blue) systems are more favorable than pure-silicates, where the zincosilicates show higher exothermicity. The aluminate ($Al(OH)_3(H_2O)$) and zincate ($Zn(OH)_2(H_2O)_2$) monomers show exothermic addition to a silicate monomer (-25.0 and -39.0 kJ/mol, respectively). In addition, the further addition of a silicate monomer is consistently exothermic in both systems, where the intermolecular attractions are stronger in the zincosilicates than aluminosilicates. In contrast to such drastic changes in the monomer addition steps, the condensation/cyclization and water removal steps are not significantly altered by the presence of aluminum or zinc. Condensation reaction energies for dimer formation are constantly around -20 kJ/mol in all systems. Trimerization reactions in aluminosilicate (-35.4 kJ/mol) and zincosilicate (-28.9 kJ/mol) species are more exothermic than that in pure-silicate (-23.5
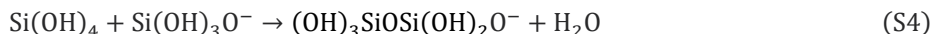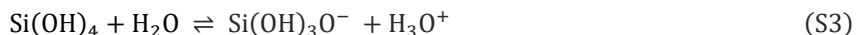
kJ/mol), but the order of exothermicity differs for tetramerization (-22.1, -10.1, and -6.9 kJ/mol for silicate, aluminosilicate, and zincosilicate, respectively). Also, cyclization reaction energies are not significantly different among systems, except for a more exothermic 4R formation in the aluminosilicate system (-26.4 kJ/mol); therefore, the effects of aluminum and zinc to the oligomerization thermodynamics are primarily attributed to the favorable intermolecular interactions between oligomers, rather than the changes in the reaction (condensation/cyclization) energies. Further, the dimerization reaction is studied in detail (Figure S13). The activation energies for the dimerization steps are 113.0, 56.4, and 15.3 kJ/mol for silicate, aluminosilicate, and zincosilicate, respectively. A linear relationship between the monomer addition energy ($\Delta G_{addition}$) and activation energy ($\Delta G^{\ddagger}$) is identified (Figure S13B) following a Brønsted-Evans-Polanyi type relationship[17]. Considering the consistent monomer addition energies throughout the pathways investigated (e.g., see Figure S12, where $\Delta G_{addition}$ is more exothermic in zincosilicates than that in aluminosilicates, whereas pure-silicates show endothermic $\Delta G_{addition}$), the linear growth kinetics (up to T) is expected to be fastest in zincosilicates, followed by aluminosilicates and slowest in pure-silicates.

2. DFT calculation in the pH-neutral environment

In this study, we use a pH-neutral environment to model (metallo-)silicate oligomerization. Zeolites are normally synthesized under basic conditions where high pH increases the solubility of silicon and aluminum sources[18, 19] and accelerates crystallization of most zeolite frameworks[19, 20]. Hence, modeling reactions under a basic environment may more accurately represent experimental findings. One way to account for the basic environment involves assuming a higher percentage of negatively charged oligomeric species produced via deprotonation by OH^- in solution phase. Mora-Fonz et al. compared the thermodynamics of oligomerization of two small silicate species with different charges (0, -1, and -2), and concluded that the reaction between a neutral species and another negatively charged species tends to be significantly more exothermic than that between two neutral species, while two negatively charged species are not likely to condense[21]. These results, however, are in contrast to the results of White et al.[22], who accurately calculated a dimerization reaction energy in high-pH conditions by coordinating the anion with water molecules and a sodium cation (Na^+) and adjusting a dielectric constant of the implicit solvent model (conductor-like screening model or COMSO[23]). They found that the reaction in a high pH condition (equation S1) is less exothermic than that under a pH-neutral condition (equation S2), although the difference was small (-9.3 and -14.2 kJ/mol, respectively).

$$Si(OH)_4 + [SiO(OH)_3^- \cdot Na^+ \cdot 3H_2O] \rightarrow [(OH)_3SiO(OH)_2O^- \cdot Na^+ \cdot 3H_2O] + H_2O \quad @\ pH = 11 \qquad (S1)$$

$$Si(OH)_4 + Si(OH)_4 \rightarrow (OH)_3SiOSi(OH)_3 + H_2O \quad @\ pH = 7 \qquad (S2)$$

Hence, we decided to carry out calculations under neutral conditions to avoid computational complexity that stems from considering multiple pathways (due to the presence of negatively charged species) and including explicit solvent molecules and cations. It should be noted that our energy diagram under the pH-neutral condition does not necessarily assume that reactions occur between charge-neutral species, which is energetically demanding (and therefore unlikely) compared to the reactions that involve anionic species[24]. In fact, anionic species exist in a neutral solution as being equilibrated with the neutral species as shown in equation S3. Therefore, a reaction between neutral species can still be assumed to occur via a pathway that involves anionic species; for example, the dimerization reaction energy (equation S2) is a sum of the reaction energies of equation S3-5.

$$Si(OH)_4 + H_2O \rightleftharpoons Si(OH)_3O^- + H_3O^+ \qquad (S3)$$

$$Si(OH)_4 + Si(OH)_3O^- \rightarrow (OH)_3SiOSi(OH)_2O^- + H_2O \qquad (S4)$$

$$(OH)_3SiOSi(OH)_2O^- + H_3O^+ \rightleftharpoons (OH)_3SiOSi(OH)_3 + H_2O \qquad (S5)$$

Indeed, the oligomerization reaction rate is maximized in weakly basic conditions, but nonetheless occurs rapidly at a neutral pH[25]. Therefore, our DFT modeling involves realistic assumptions and is used to reveal trends in zeolite oligomerization chemistry in the presence of aluminate and zincate species, rather than

calculate accurately the energetics of each elementary steps of charged species in solution. pH-neutral DFT calculations were also used in a recent work to investigate oligomerization thermodynamics of (alumino)silicates, and successfully described the effects of various factors (including Si/Al ratio and the presence of a cation (Na^+ and Ca^{2+})) in the early stage of zeolite growth[12].

3. Computational models of ONIOM calculation

The ONIOM method can accurately model chemistry on zeolite frameworks with a reasonable computational cost[15, 26, 27-29]. Adequate partitioning is crucial to an accurate chemical description, which depends on the size of the system, computational method(s), objective(s) of study, etc. For example, Gomes et al.[27] reported that having 5 T-sites (tetrahedral sites) on the adsorption site in a high layer provides accurate adsorption energy of hydrocarbons on a MFI zeolite. On the other hand, Li and coworkers[28] found that 8 T-sites in a high layer of a two-layered ONIOM calculation scheme is insufficient to accurately describe a Brønsted acid site, so it is necessary to include more T-sites in the high layer or add an intermediate layer. Montejo-Valencia et al.[29] investigated tin and titanium substitution on different zeolite frameworks and calculated Brønsted acidity with ONIOM calculations, with a relatively large high-layer size (more than 5 nearest neighbors of the substitution site). The substitution energies of Al and Zn ($\Delta E_{substitution}$) (Figures 7a and S18) were calculated as follows:

$$\Delta E_{substitution} = E_{Al\ (or\ Zn)-zeolite} + E_{Si(OH)_4} - E_{pure-silicate\ zeolite} - E_{Al\ (or\ Zn)\ monomer} \quad \text{(S6)}$$

where E indicates the electronic energy of a species.

In our ONIOM (M062X/6-311g(d,p):PM6) calculations, a sufficient number of atoms surrounding the substitution T-site should be included in the high layer to account for effects from local environments (i.e., bulk and surface). Hence, we constructed three partitioning schemes, which are named 'small', 'medium', and 'large' depending on the number of atoms in the high layer, as presented in Figure S16. In the 'small' partitioning scheme, each location has 8 T-sites in the high layer. Both in the FAU and GIS structures, 56 atoms are included in the high layer. In the 'medium' scheme, the number of T-sites increases to 12 and 16 in surface and bulk locations, respectively. The surface high-layered location has fewer T-sites than bulk since the surface is pruned. However, there are greater number of atoms in surface due to the presence of terminal hydrogen atoms. The numbers of atoms that belong to the high layer are 80 and 74 in the FAU and GIS structures, respectively. Finally, to prepare the 'large' scheme, we included more oxygen and hydrogen atoms into the high layer while maintaining the number of T-sites, leading to 96 and 94 high-layer atoms in the FAU and GIS structures, respectively.

Aluminum and zinc substitution energies calculated with the different partitioning schemes are shown in Figure S18. It is worth noting that the aluminum substitution energy in the bulk location is unreasonably high in both frameworks of the small partition scheme. This is due to the formation of an unrealistic Al (in high layer) – Si (in low layer) bond during optimization. Therefore, the small partitioning scheme does not have sufficient number of atoms in the high ONIOM layer. On the other hand, all substitution energies in the medium and large partition schemes show thermodynamic trends that remain consistent. Substitution energies determined with the large partitioning scheme are reported in the main manuscript with the rest reported in Figure S18.

## 4. Local geometry environment on substitution sites

Here, we provide a more detailed analysis of geometric changes upon Al and Zn substitution into the surface and bulk locations of the FAU framework. Structures used in our analysis correspond to the "large" ONIOM partitioning scheme. As described in the manuscript, one or two protons are added to first oxygen-neighbors after substitution to compensate for negative charges emerging from replacing a tetravalent silicon atom by a trivalent (Al) or divalent (Zn) atom. T-O bonds are observed to elongate after substitution, which is more significant on Brønsted-acidic oxygens. This nonuniform bond elongation breaks the symmetry of the nearly regular SiO_4 tetrahedron. We quantified the distortion based on the percent deviation of the oxygen atom positions from their positions in a corresponding regular tetrahedron, determined using PolyDis

package developed by D. Stoiber and R. Niewa[30]. For the calculation, a center of gravity of the four oxygen atoms is found in the Cartesian coordinate system, by which each oxygen position can be defined as a 3D vector relative to this center. Then, the vectors representing the vertices of the original (distorted) tetrahedron are determined by having the average length of 1 (called $\overrightarrow{P_n}$, where n = 1–4). Also, the unit vectors representing the vertices of a regular tetrahedron ($\overrightarrow{P_n^*}$) are determined and the sum of the distance of each vertex to its ideal position is minimized while maintaining the shape of a regular tetrahedron for $\overrightarrow{P_n^*}$. Finally, the corresponding percent distortion (D) is determined as the sum of the distance between two vectors divided by the sum of the distance of each vertex to the center of gravity (= 4). This can be represented by equation S7:

$$D = \frac{\min\left(\Sigma_1^n\left(\left|\overrightarrow{P_n^*P_n}\right|\right)\right)}{\Sigma_1^n\left(\left|\overrightarrow{P_n}\right|\right)} \cdot 100(\%) \tag{S7}$$

Detailed formulas and descriptions can be found in ref.[30]. Figure S19 shows the distorted tetrahedron upon substitution superimposed to the corresponding regular tetrahedron (scaled to match the bond lengths of the original tetrahedron). For aluminum substitution, one Al – O distance is longer than the others by ~0.17 Å, resulting in minor distortions (3.8 and 4.9% in bulk and surface, respectively; see Table S3). On the other hand, two Zn-O bonds in the zincate tetrahedron are longer than the others by >0.2 Å; therefore, these T-sites deviate substantially from their regular positions. Zinc substitution on a surface site leads to more deviation than that in a bulk site (14 and 16% in bulk and surface, respectively). The more significant distortion for surface sites can be attributed to their distinct local coordination environment. Namely, in contrast to the bulk location, which is in the middle of crystalline structure, half of the covalent network (beyond first-neighbor oxygens) is absent surrounding the surface T-site. Hence, surface locations are less resistant to distortions compared to bulk locations, resulting in significantly more exothermic Zn substitution in surface sites compared to bulk sites (see Figure 7 in the manuscript). Significant distortion upon zinc substitution is also observed on the GIS framework as illustrated in Figure S20.
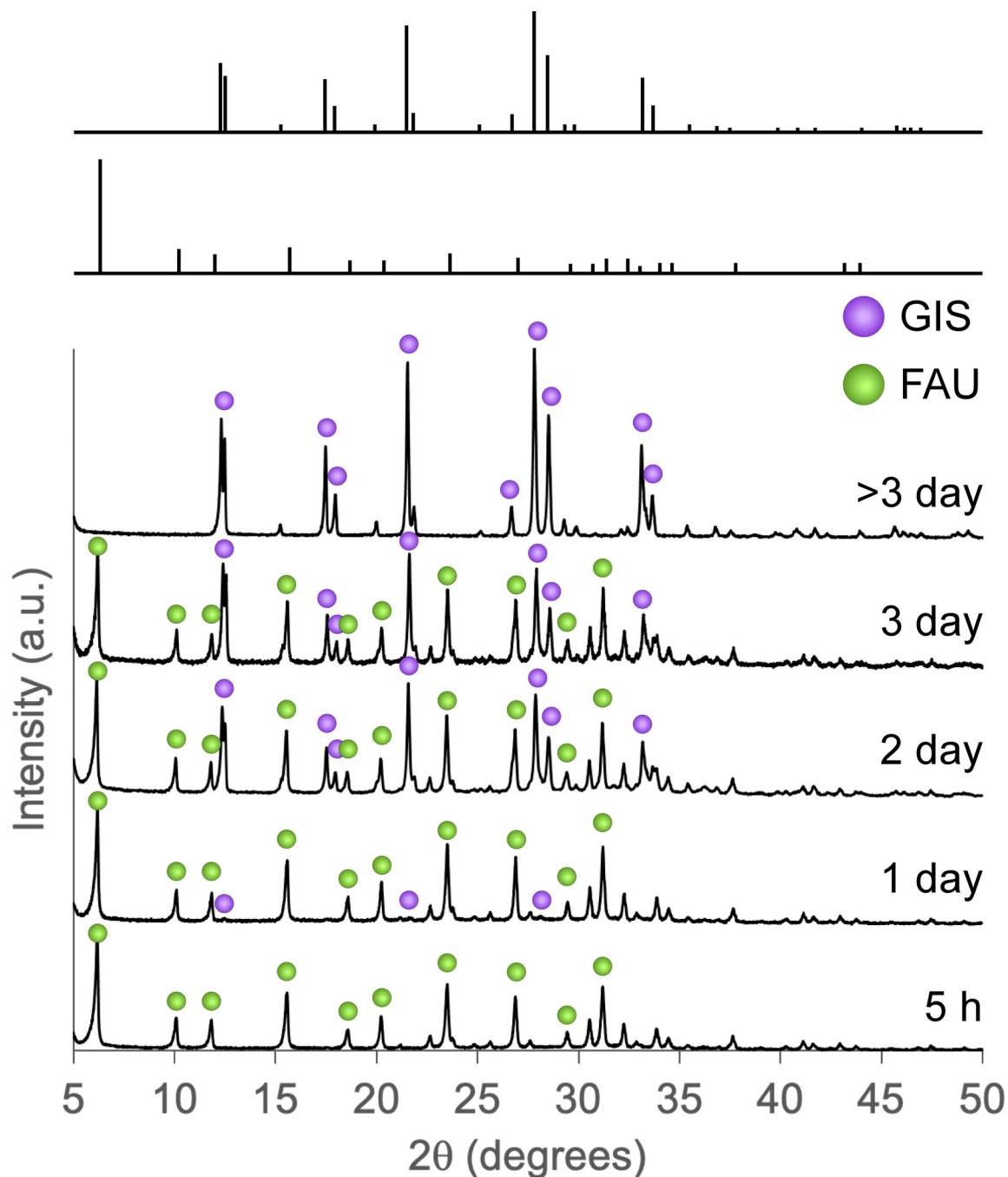
Figure S1. Time-elapsed powder XRD patterns depicting the FAU-to-GIS interzeolite transformation for samples synthesized at 100°C for 0 – 7 days. All samples were prepared using a growth mixture with a molar composition of 9 SiO_2:0.5 Al_2O_3:11 NaOH:190 H_2O. Select peaks are indicated using green (FAU) or purple (GIS – P2) circles. Reference patterns of GIS – P2 (top) and FAU (bottom) obtained from the International Zeolite Association Structure Database are displayed.
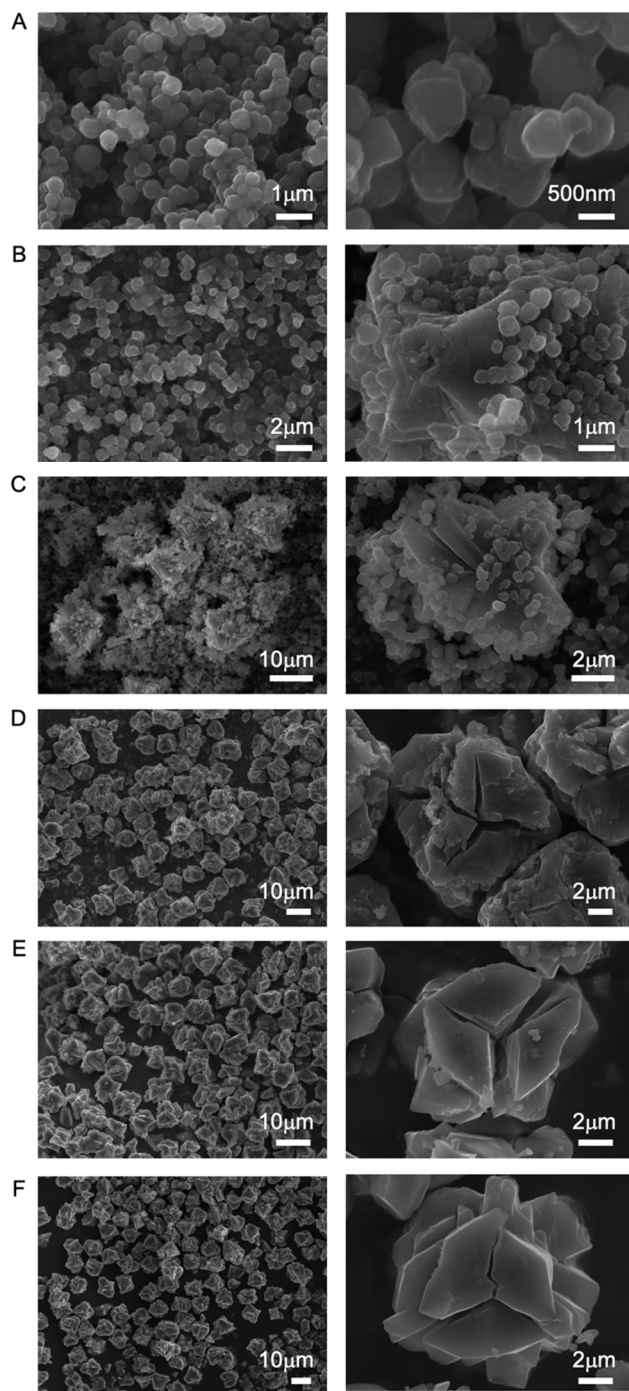
Figure S2. Scanning electron micrographs depicting the FAU-to-GIS interzeolite transformation for products synthesized at 100°C for (A) 4 h (FAU), (B) 1 day (FAU with GIS impurity), (C) 2 days (mixed FAU and GIS), (D) 4 days (GIS), (E) 7 days (GIS), and (F) 8 days (GIS). All samples were prepared using a growth mixture with a molar composition of 9 SiO_2:0.5 Al_2O_3:11 NaOH:190 H_2O. All products containing GIS are polymorph P2.
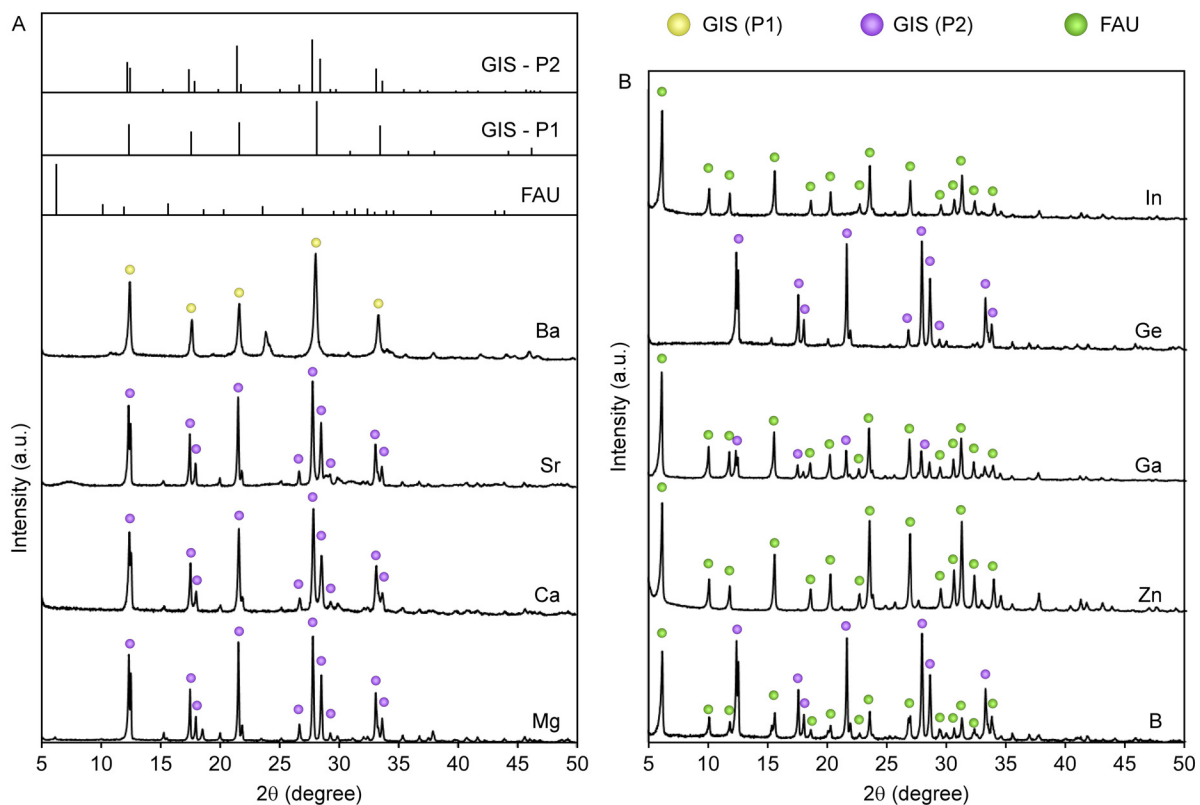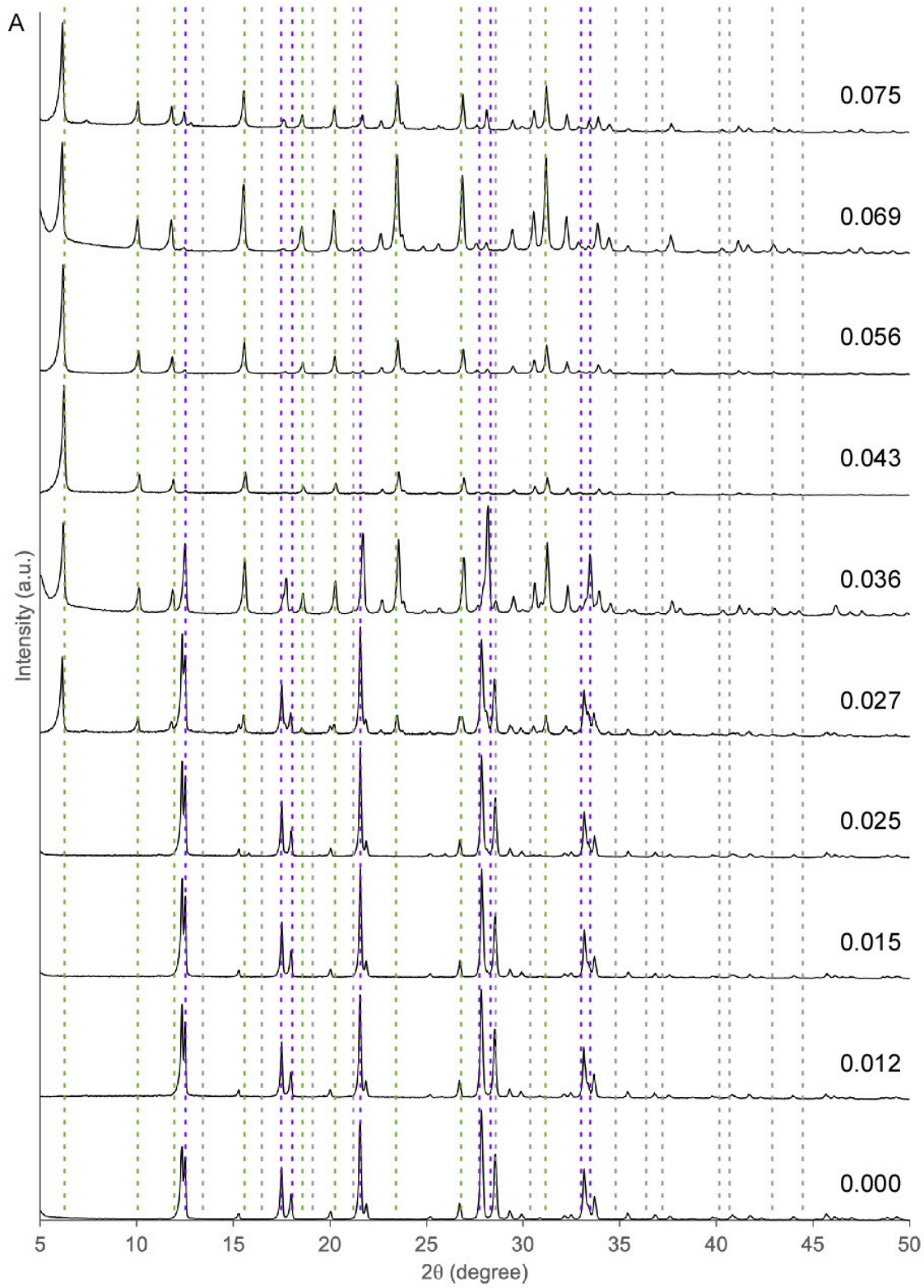
Figure S3. Powder XRD patterns of zeolite products synthesized at 100°C for 4 days. All samples were prepared using a growth mixture with a molar composition of 9 SiO_2:0.5 Al_2O_3:0.2 M:11 NaOH:190 H_2O, where *M* represents the multivalent species indicated on the right-hand side of each pattern. Select peaks are indicated using green (FAU), yellow (GIS – P1) or purple (GIS – P2) circles. Reference patterns of GIS – P2 (top), GIS – P1 (middle), and FAU (bottom) obtained from the International Zeolite Association Structure Database are displayed.
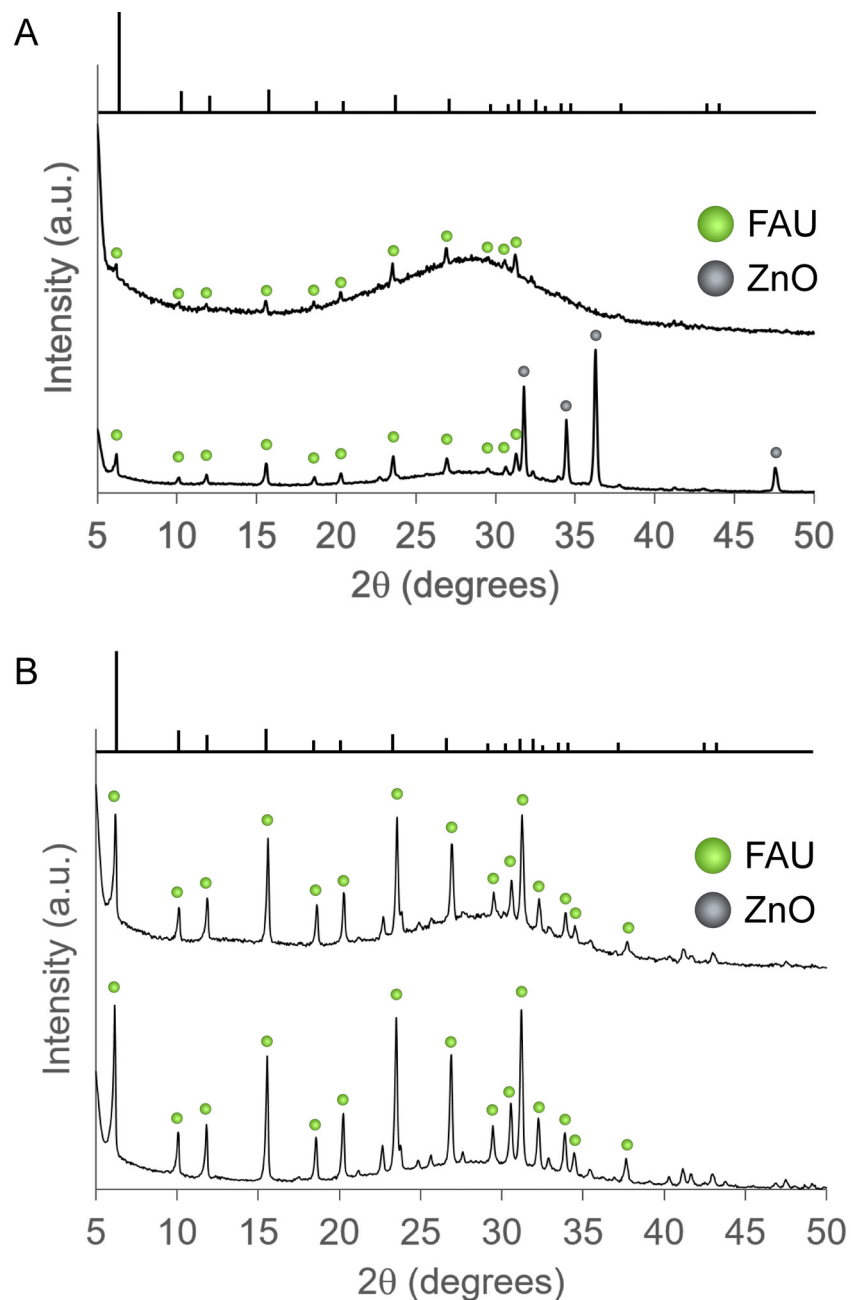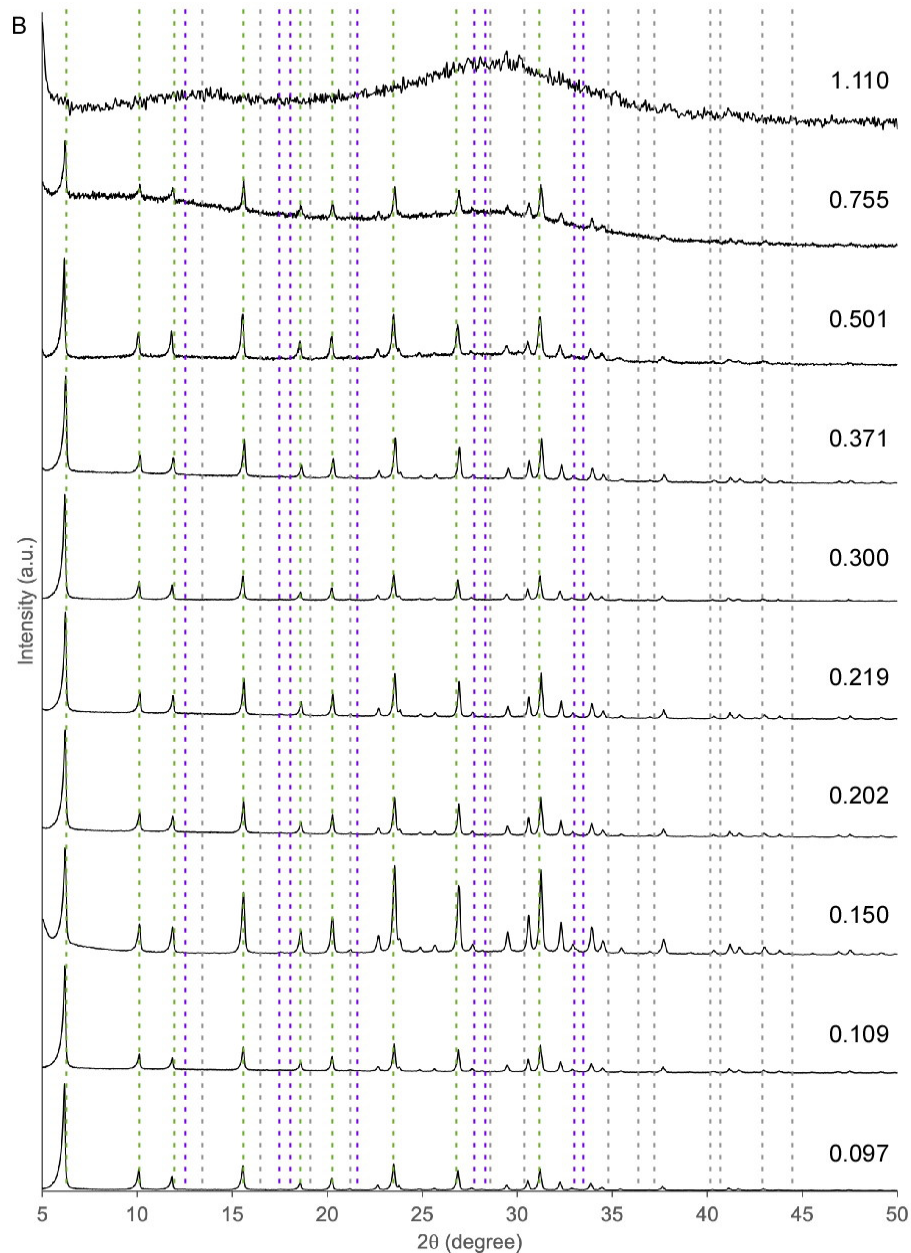
Figure S4. Powder XRD patterns of samples with mixed amorphous and crystalline (FAU) phases synthesized in the presence of different zinc sources: $Zn(NO_3)_2$ (top) and ZnO (bottom). Variations in product peak intensities indicate a minimal anion effect on crystallization rates. (A) Samples were prepared using a growth mixture with a molar composition of 9 SiO_2:0.5 Al_2O_3:0.7 Zn:11 NaOH:190 H_2O and hydrothermal treatment at 100°C for 3 days to assess the effect of zinc on the FAU-to-GIS interzeolite transformation for a conventional synthesis time. (B) Samples were prepared using a growth mixture with a molar composition of 9 SiO_2:0.5 Al_2O_3:0.5 Zn:11 NaOH:190 H_2O and hydrothermal treatment at 100°C for 28 days to assess the effect of zinc on the FAU-to-GIS interzeolite transformation at extended synthesis times. A reference pattern of FAU obtained from the International Zeolite Association Structure Database is displayed.
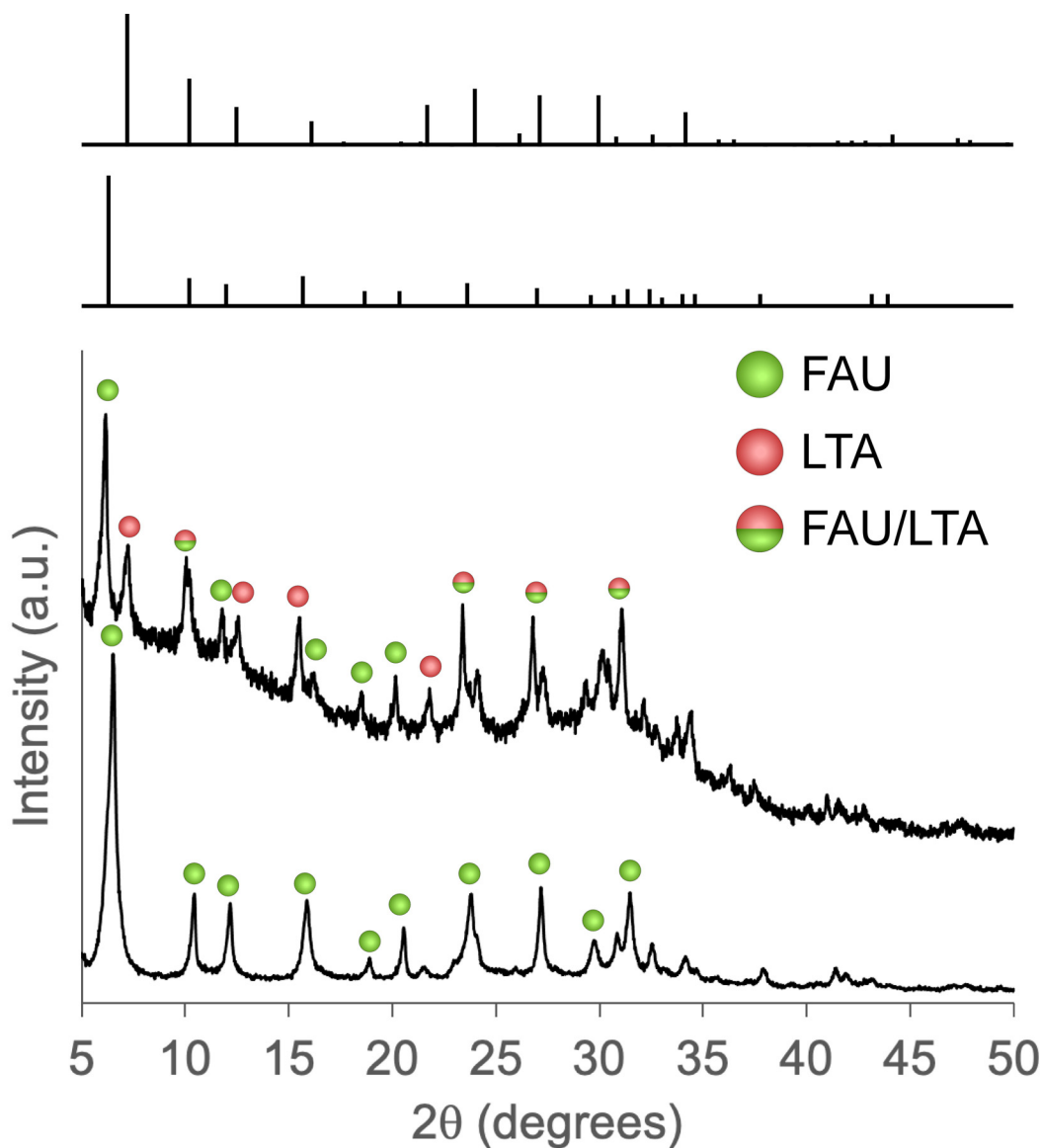
Figure S5. Powder XRD patterns of products with mixed FAU and LTA phases. Samples were prepared using a growth mixture with a molar composition of 12 SiO_2:5 Al_2O_3:x Zn:11 NaOH:190 H_2O where $x = 0$ (bottom) or $x = 1.3$ (top). Samples were treated at 65°C (top) or 100°C (bottom) for 7 days. The presence of a more significant LTA phase in the latter product suggests that zinc leads to synthesis mixtures with effectively lower Si/Al ratios. Select peaks are indicated using green (FAU), red (LTA), or mixed circles. Reference patterns of LTA (top) and FAU (bottom) obtained from the International Zeolite Association Structure Database are displayed.

Figure S6. (A and B) Powder XRD patterns for samples prepared using a growth mixture with a molar composition of 9 SiO_2:0.5 Al_2O_3:x Zn:11 NaOH:190 H_2O. All samples were hydrothermally treated at 100°C for 5 days. The value of x is indicated on the right side of each corresponding XRD pattern. Dashed lines indicate select crystalline peaks of FAU (green), GIS – P2 (purple), and hemimorphite (gray)[31]. For clarity, the figure is split into panels (A) (0 < x < 0.075) and (B) (0.097 < x < 1.110). We have analyzed the full width half maximum (FWHM) of the 5 largest FAU peaks for crystals obtained in the presence of different amounts of zinc. We observe an increase in the FWHM value at higher zinc loadings for select peaks (e.g. 23.55, 26.90, and 31.25 degrees) that does not occur for smaller angle peaks; however, attributing these changes to any specific siting of Zn in the FAU framework is nontrivial.
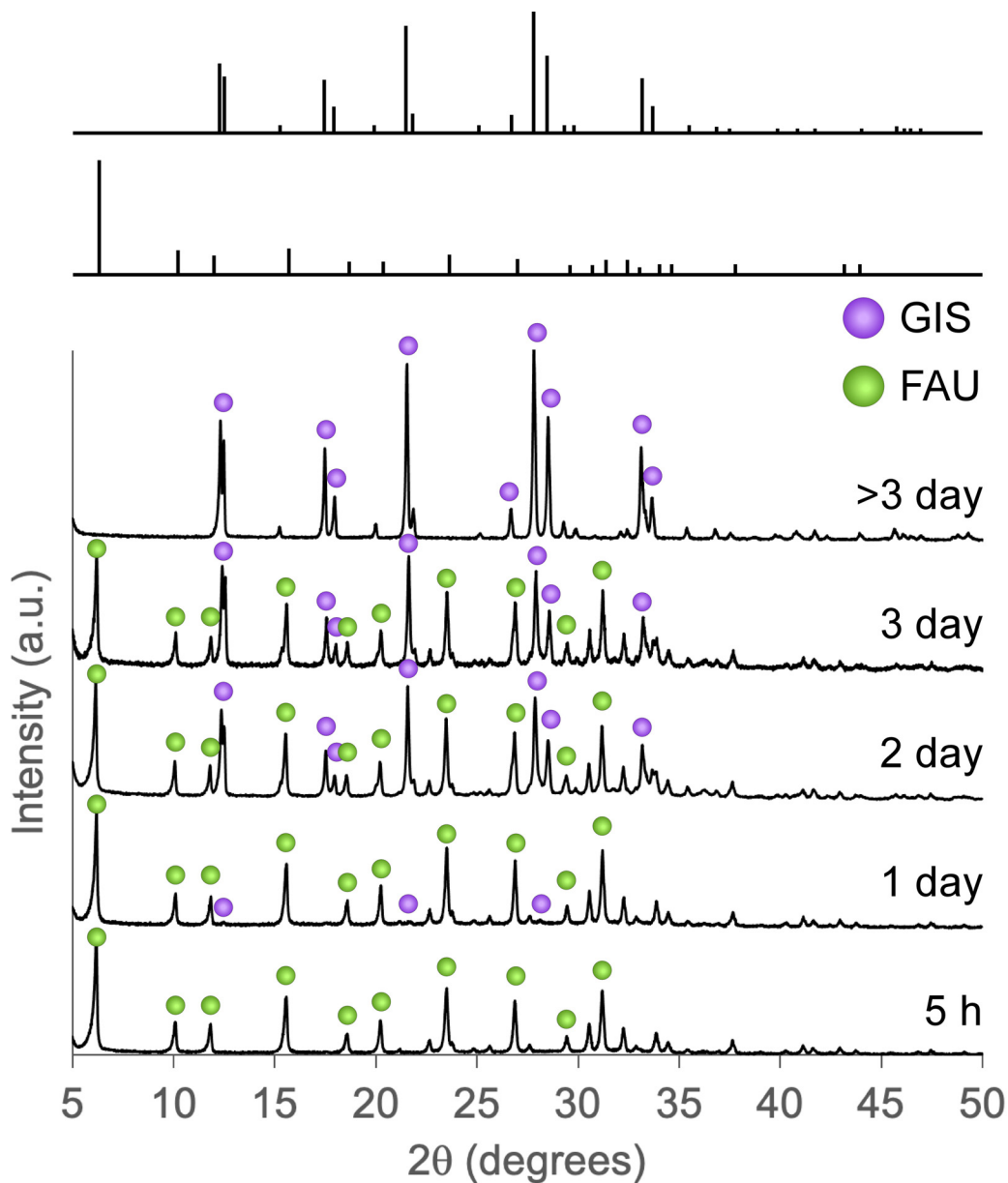
Figure S7. Powder XRD patterns for samples prepared using a growth mixture with a molar composition of 9 SiO_2:0.5 Al_2O_3:11 NaOH:190 H_2O. All samples were hydrothermally treated at 100°C for 7 days with mid-synthesis addition of Zn at a molar ratio of 0.2. The time of Zn addition is indicated on the right side of each corresponding XRD pattern. After 3 days (top), fully crystalline GIS is formed, whereupon mid-synthesis Zn addition has no noticeable effect on the product. Select peaks are indicated using green (FAU) or purple (GIS) circles. GIS peaks correspond to polymorph P2 with the possible exception of a minor zeolite P1 phase when Zn is added after 2 days. Reference patterns of GIS – P2 (top) and FAU (bottom) obtained from the International Zeolite Association Structure Database are displayed.
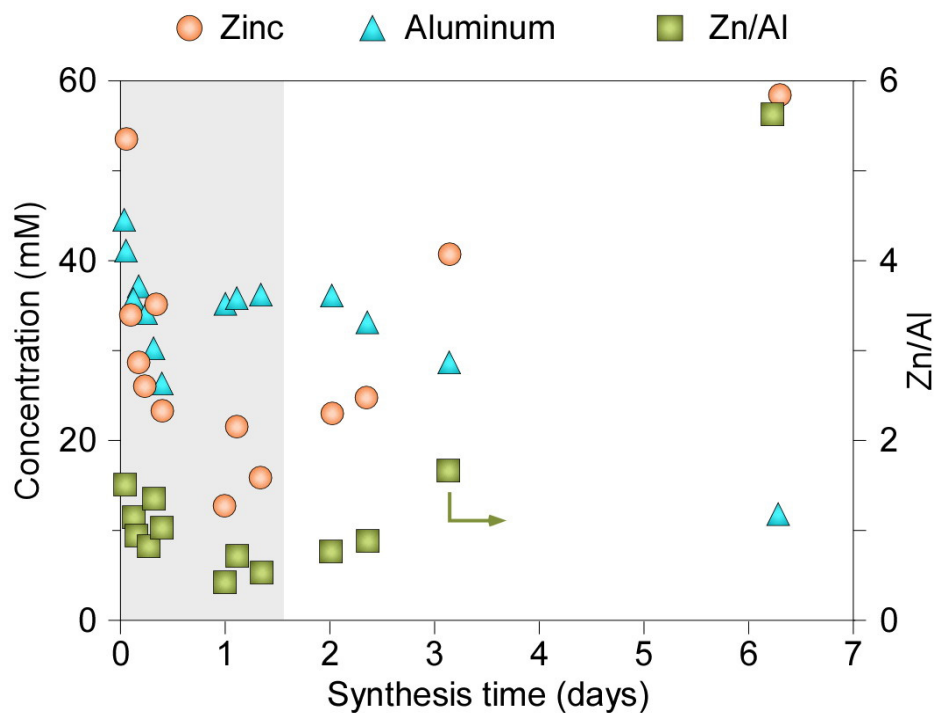
Figure S8. Elemental analysis of supernatant solutions extracted at periodic times during a synthesis at 80°C using a molar composition of 9 SiO_2:0.5 Al_2O_3:0.2 Zn:11 NaOH: 190 H_2O. Here we report the concentration of zinc (orange circles) and aluminum (aqua triangles) in solution. Compositions were measured by ICP-MS. The induction period (shaded gray region) corresponds to powder XRD patterns of extracted solids without visible appearance of Bragg peaks. Nucleation was observed around 1.7 days with full crystallinity of FAU attained around 6 days. A comparison of Al evolution for samples with/without Zn is shown in Figure S9.
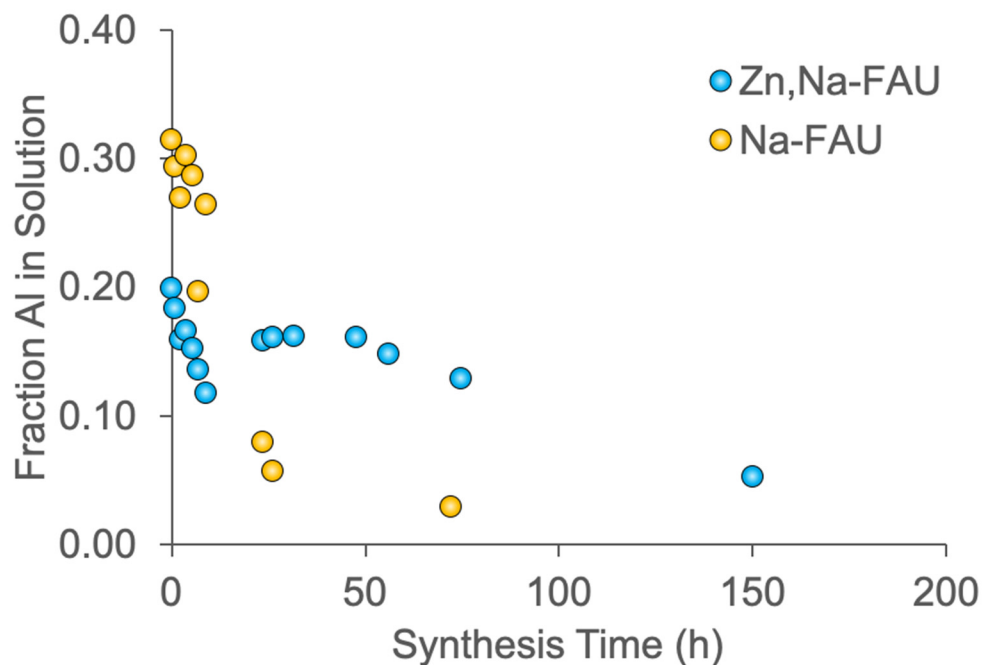
Figure S9. Time-resolved compositional analysis of Al concentration in the supernatant from FAU zeolite syntheses in the presence (blue) and absence (yellow) of zinc. Growth mixtures were prepared using a molar composition of 9 SiO_2:0.5 Al_2O_3:x Zn:11 NaOH:190 H_2O where $x = 0.35$ (blue) or $x = 0$ (yellow) and were hydrothermally treated at 80°C with aliquots removed periodically. Supernatant concentration was measured using inductively coupled plasma mass spectroscopy (ICP-MS) after isolating and diluting the supernatant from the aliquoted sample.
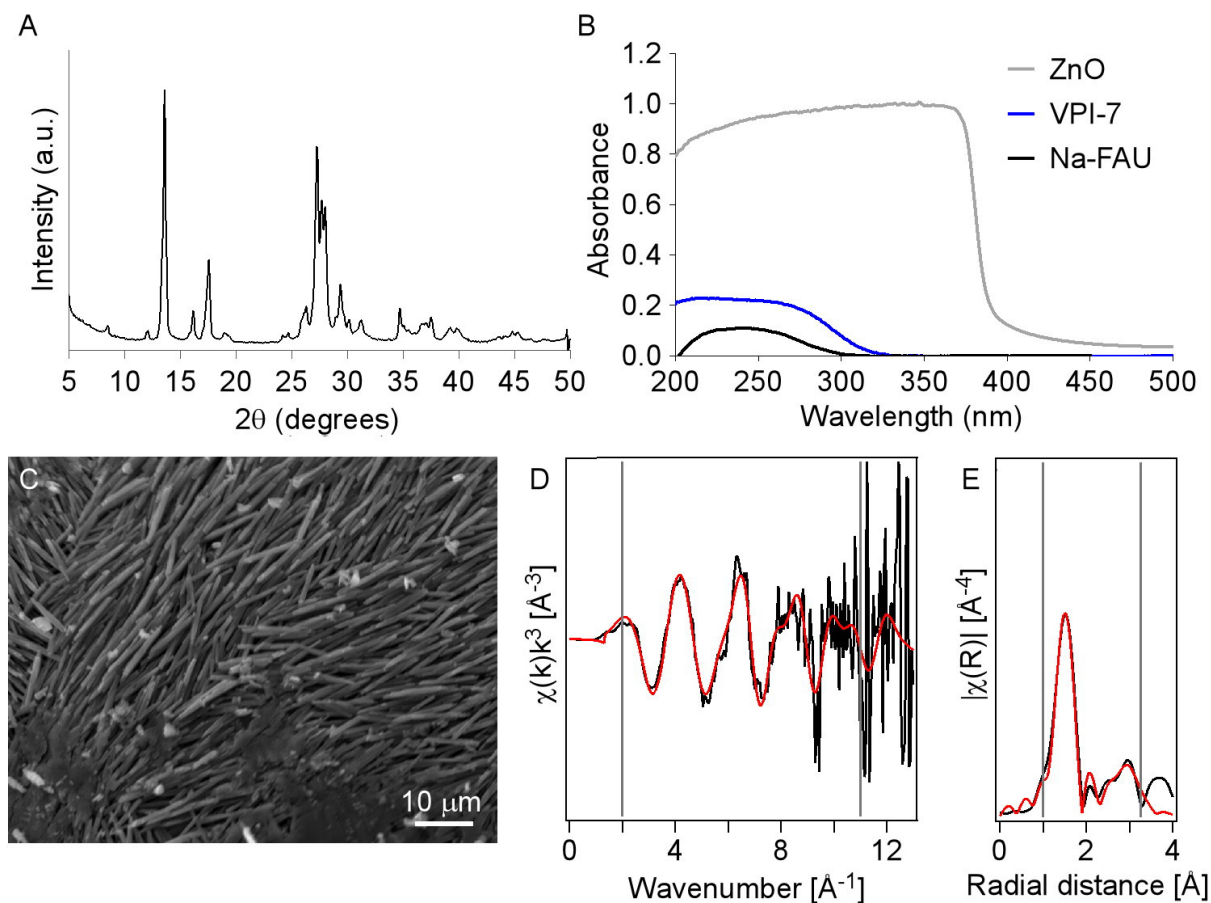
Figure S10. (A) Powder XRD pattern of VPI-7 (VSV type) prepared using a growth mixture with a molar composition of 9 SiO_2:0.6 Zn:11 NaOH:190 H_2O and hydrothermally treated at 150°C for 7 days. (B) UV-Vis spectra of Na-FAU (black), VPI-7 (blue), and commercial ZnO (gra) as a reference. (C) Scanning electron micrograph of VPI-7 zincosilicate crystals. (D) Zn K-edge EXAFS spectra (black) for solid precipitate. Shell-by-shell fits (red) were produced using a hemimorphite reference structure. Fitting metrics are presented in Table S1. (E) Fourier transforms of the Zn EXAFS data. Gray lines define the fit window of (D) 2 - 11 Å^{-1} and (E) 1 - 3.25 Å.

	Pure-silicate	**Aluminosilicate**	**Zincosilicate**
M	$Si(OH)_4$	$Al(OH)_3(H_2O)$	$Zn(OH)_2(H_2O)_2$
D	$Si_2O(OH)_6$	$SiAlO(OH)_5(H_2O)$	$SiZnO(OH)_4(H_2O)_2$
Tr	$Si_3O_2(OH)_8$	$Si_2AlO_2(OH)_7(H_2O)$	$Si_2ZnO_2(OH)_6(H_2O)_2$
3R	$Si_3O_3(OH)_6$	$Si_2AlO_3(OH)_5(H_2O)$	$Si_2ZnO_3(OH)_4(H_2O)_2$
T	$Si_4O_3(OH)_{10}$	$Si_3AlO_3(OH)_9(H_2O)$	$Si_3ZnO_3(OH)_8(H_2O)_2$
(3-1)R	$Si_4O_4(OH)_8$	$Si_3AlO_4(OH)_7(H_2O)$	$Si_3ZnO_4(OH)_6(H_2O)_2$
4R	$Si_4O_4(OH)_8$	$Si_3AlO_4(OH)_7(H_2O)$	$Si_3ZnO_4(OH)_6(H_2O)_2$
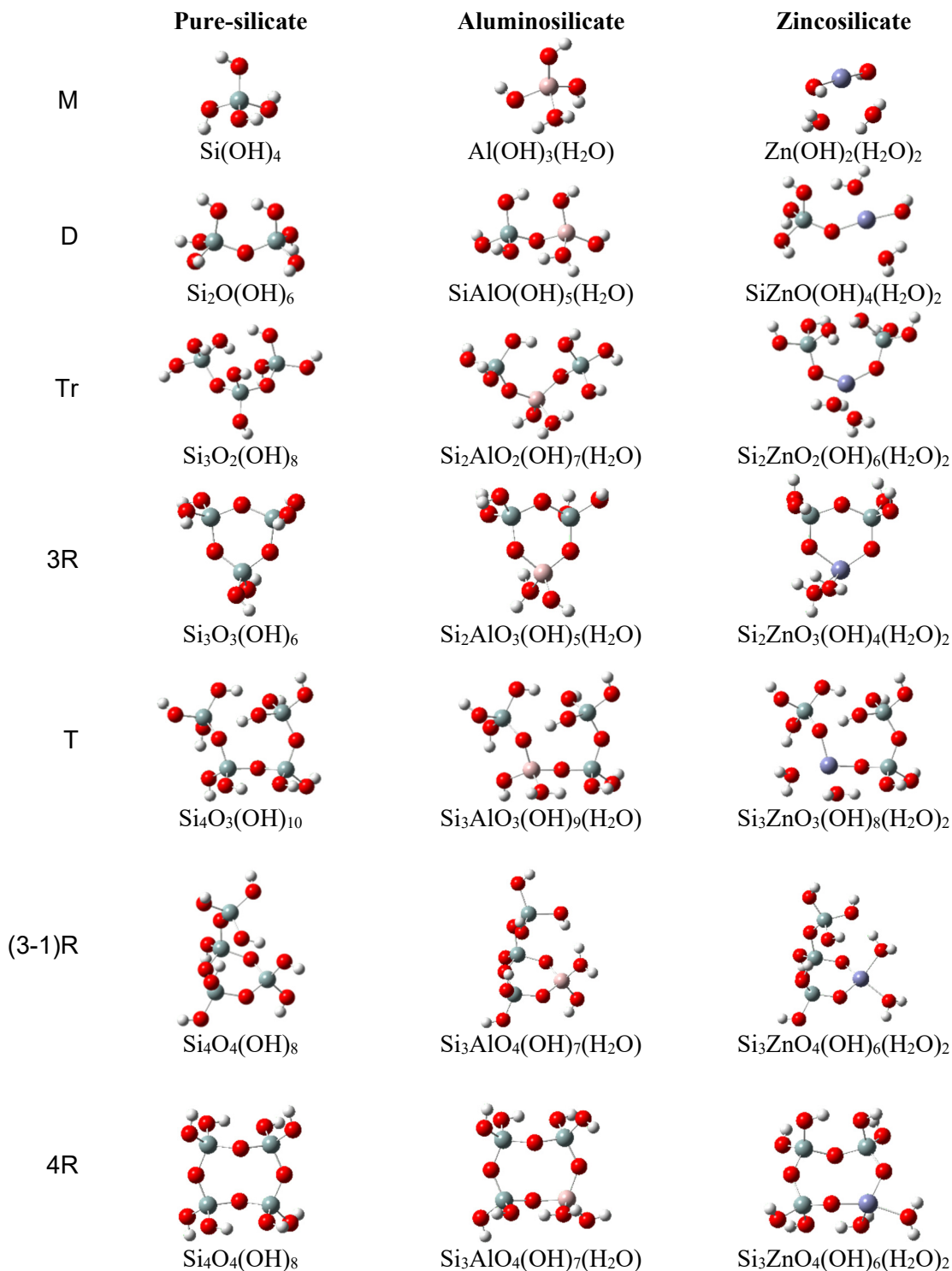
Figure S11. Species investigated in the computational studies of oligomerization. Linear species are monomer (M), dimer (D), linear trimer (Tr), and linear tetramer (T). Cyclic species are 3-membered ring (3R), 3-membered ring with one acyclic silicon ((3-1)R), and 4-membered ring (4R). In molecular structures, balls are color coded according to element: silicon (gray), aluminum (pink), zinc (purple), oxygen (red), and hydrogen (white).
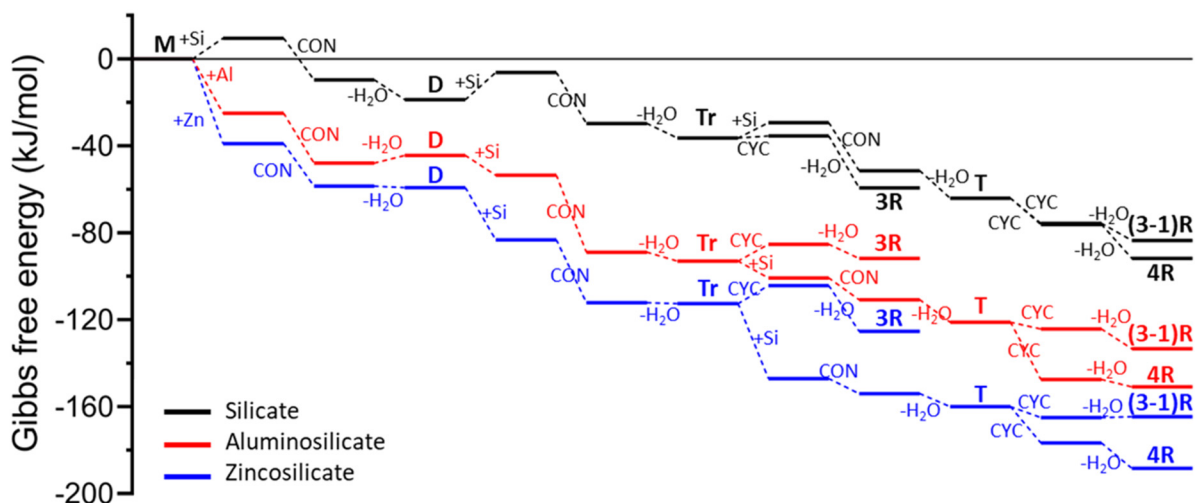
Figure S12. Gibbs free energy profiles of oligomerization of pure-silicate (black), aluminosilicate (red), and zincosilicate (blue) species up to the formation of the tetrameric species (i.e. containing 4 tetrahedral units) calculated using DFT. Beginning with a silicate monomer (M), we quantify the energy of growth to dimer (D), linear trimer (Tr), and linear tetramer (T) species. Cyclic structures investigated include 3-member ring (3R), 3-member ring with one acyclic silicon ((3-1)R), and 4-member ring (4R). The optimized molecular structures are shown in Figure S11. The addition steps of silicate, aluminate, and zincate monomers are represented by "+Si", "+Al", and "+Zn", respectively. Other reaction steps include condensation (CON), cyclization (CYC), and water removal (-H$_2$O).
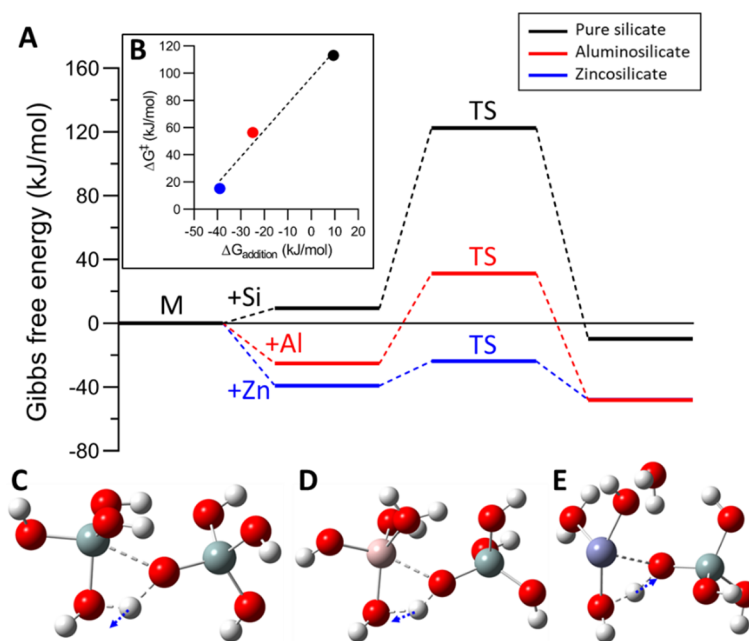
Figure S13. (A) Detailed dimerization energetics of pure-silicate (black), aluminosilicate (red), and zincosilicate (blue), beginning with a silicate monomer (M). The addition steps of silicate, aluminate, and zincate monomers are represented by "+Si", "+Al", and "+Zn", respectively. "TS" stands for transition state. (B) Linear relationship between monomer addition energy ($\Delta G_{addition}$) and activation energy ($\Delta G^{\ddagger}$). Optimized transition state structures of (C) pure-silicate, (D) aluminosilicate, and (E) zincosilicate, with the dotted lines showing bonds being formed/broken at the transition state.
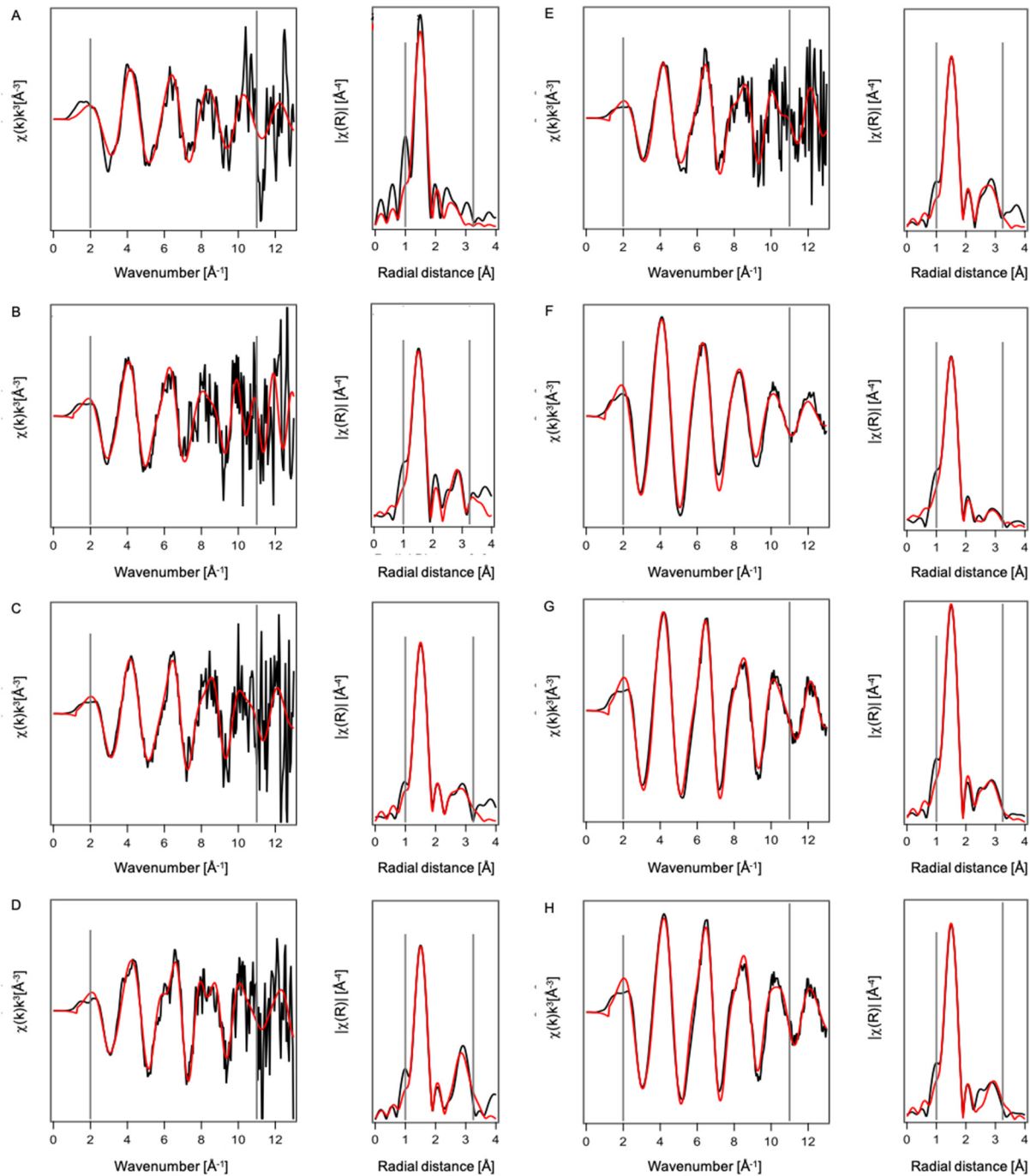
Figure S14. EXAFS measurements of Zn,Na-FAU samples with various Zn/Al ratios, which are shown in Table S1 for (A) Zn,Na-FAU-2, (B) Zn,Na-FAU-3, (C) Zn,Na-FAU-4, (D) Zn,Na-FAU-5, (E) Zn,Na-FAU-6, (F) Zn,Na-FAU-7, and (G) Zn,Na-FAU-8. Sample Zn,Na-FAU-8 was also fit without Si in the model, and the results of this fit are shown in panel H for comparison. In each panel, there are 2 graphs: (Left) Zn K-edge EXAFS spectra (black) for Zn,Na-FAU samples. Shell-by-shell fits (red) were produced using FAU framework or hemimorphite reference structures (Table S1). (Right) Fourier transforms of the Zn EXAFS data. Gray lines define the fit window of 2 - 11 Å^{-1} (k space) and 1 - 3.25 Å (R space).
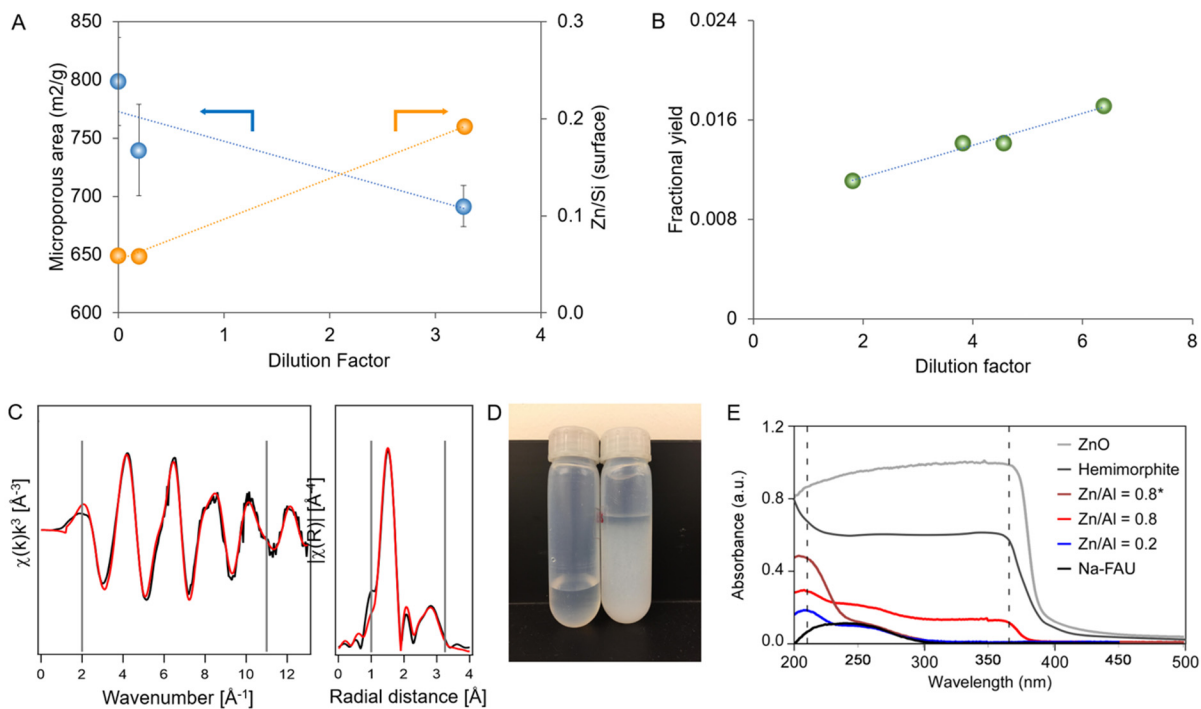
Figure S15. Analysis of solid precipitate that forms upon diluting the supernatant of Zn,Na-FAU syntheses after hydrothermal treatment. (A) Properties of Zn,Na-FAU are affected by the amount of DI water added to the growth mixture post-synthesis: BET surface area (blue) monotonically decreases concurrently with a monotonic increase in the Zn/Si ratio at the crystal surface (yellow), which is analyzed using XPS. Dilution factor is equivalent to M_w/M_z where M_w is the mass of water added and M_z is the mass of the zeolite growth mixture. (B) Solid yield when DI water is added to isolated supernatant solution. Fractional yield is equivalent to M_p/M_s where M_p is the mass of solid precipitate and M_s is the mass of the supernatant solution. (C) (Left) Zn K-edge EXAFS spectra (black) for solid precipitate. Shell-by-shell fits (red) were produced using a hemimorphite reference structure. Fitting metrics are presented in Table S1. (Right) Fourier transforms of the Zn EXAFS data. Gray lines define the fit window of 2 - 11 Å^{-1} (k space) and 1 - 3.25 Å (R space). (D) Photograph of isolated supernatant solutions from Zn,Na-FAU growth mixtures immediately before (left) and after (right) dilution with ~30 mL of DI water. This image depicts the rapid precipitation of zincosilicate solid. (E) UV-Vis spectra of zeolite samples and reference materials. When samples are washed with deionized water (i.e., diluted) prior to decanting the supernatant (Zn/Al = 0.8), we observe two peaks (210 and 365 nm) where the latter is characteristic of either zinc oxide or hemimorphite. When samples are washed after decanting (i.e. disposing of) the supernatant (Zn/Al = 0.8*), the longer wavelength peak (365 nm) is absent.
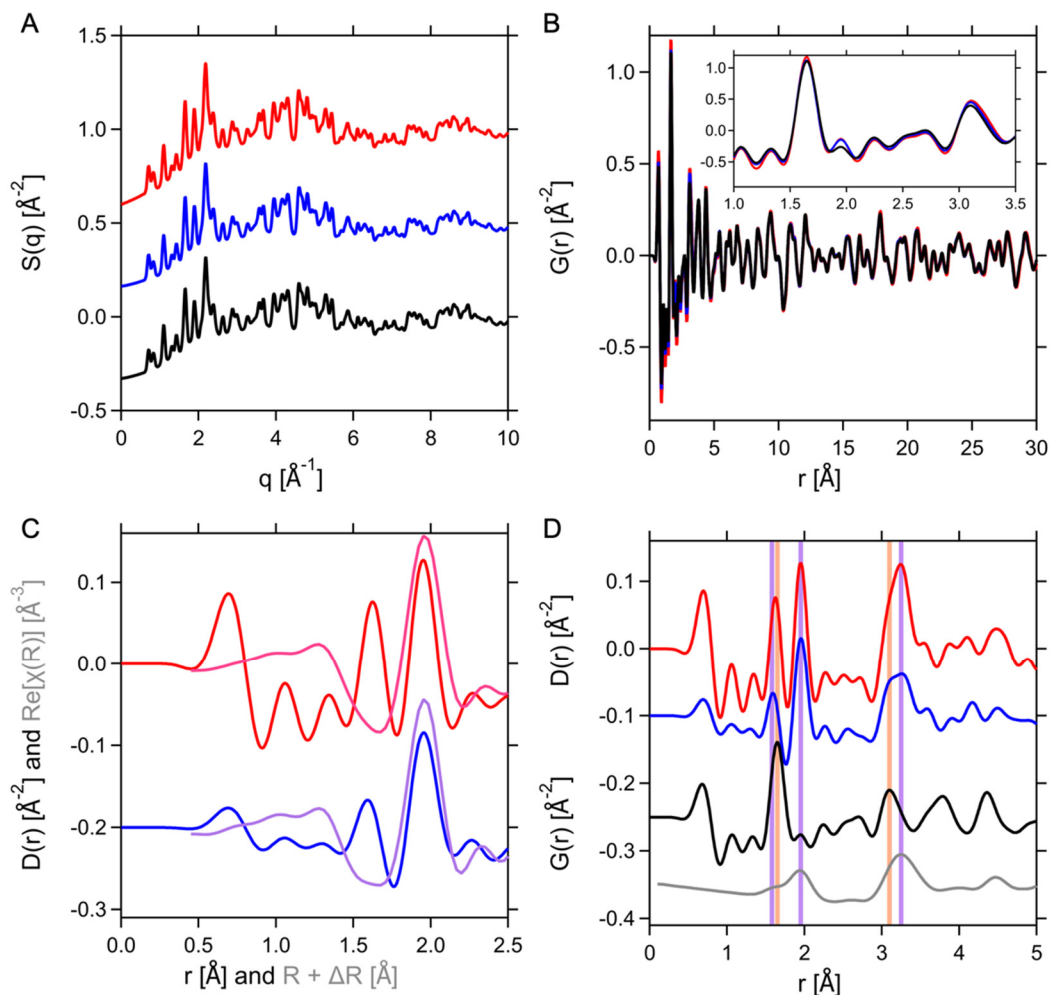
Figure S16. (A) Total structure factor measurement of three samples, Na-FAU (black), Zn,Na-FAU (Zn/Al = 0.2) (blue), and Zn,Na-FAU (Zn/Al = 0.8) (red), demonstrating that materials are crystalline FAU. (B) X-ray PDF profiles of Na-FAU (black), Zn,Na-FAU (Zn/Al = 0.2) (blue), and Zn,Na-FAU (Zn/Al = 0.8) (red). Inset is a magnification of the region from 1 to 3.5 Å. Direct comparison of PDF profiles shows the Zn-associated differences in structure are primarily located at distances < 10 Å. (C) Differential X-ray pair distribution function (dPDF) profiles from 0 to 2.5 Å overlaid with real parts of Zn EXAFS (see Figure 6 in the manuscript). Zn,Na-FAU (Zn/Al = 0.2) shown in blue is overlaid with the EXAFS spectrum (purple) for the same sample. Zn,Na-FAU (Zn/Al = 0.8) shown in red is overlaid with the EXAFS spectrum (purple) for the same sample. This comparison demonstrates the peaks at ≈1.62 Å are not part of the Zn coordination and likely correspond to a Si/Al − O atom pair associated with the Zn-induced defect structure. (D) dPDF profiles of Zn,Na-FAU samples compared to the scaled G(r) profiles of faujasite (black) and hemimorphite (gray), calculated from ICSD entry 30012[32]. Orange lines highlight major atom pairs in the FAU structure, lavender lines highlight structural features of hemimorphite.
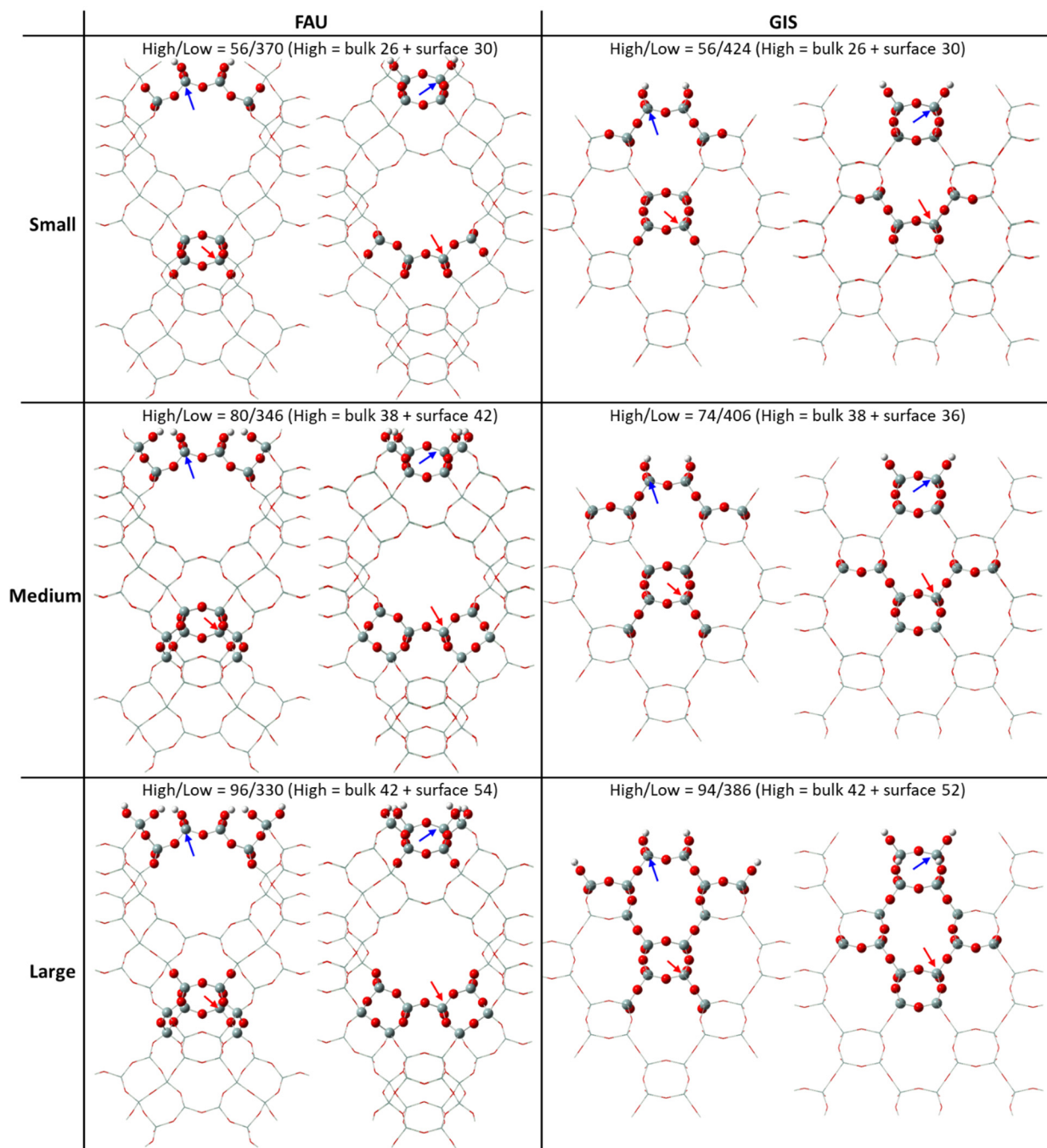
Figure S17. 2-layer ONIOM schemes for FAU and GIS zeolite frameworks at three different levels of partitioning (small, medium, and large) based on the number of atoms in the high layer (DFT calculation, ball and stick). The high level is treated with M062X/6-311g(d,p) and the low level with PM6. The atoms represented by wires are calculated by the low layer. The T-sites for substitution in the bulk and surface are highlighted by red and blue arrows, respectively.
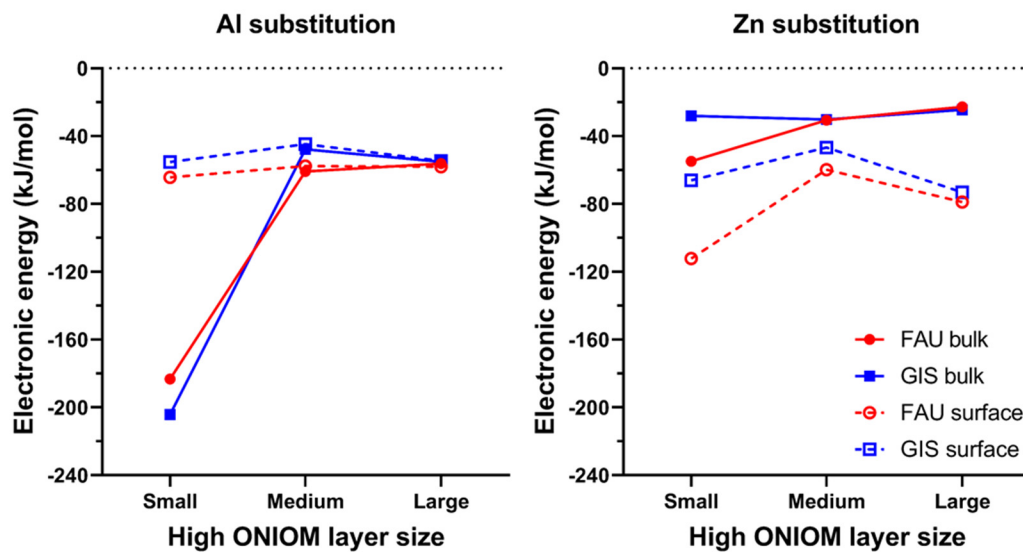
Figure S18. Electronic energies of Al- (left) and Zn- (right) substitution in bulk (closed symbols) and surface (open symbols) locations on FAU (red) and GIS zeolite frameworks (blue) calculated using the three different ONIOM partitioning schemes.
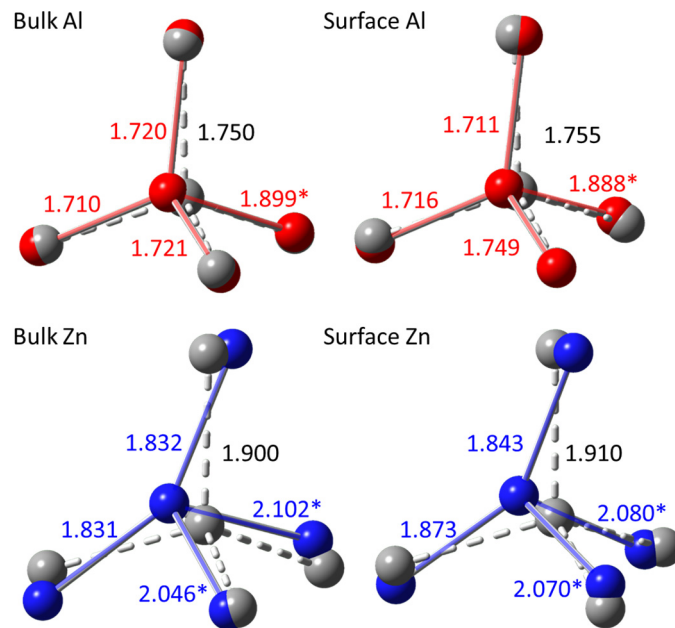
Figure S19. Aluminate (AlO$_4$, red) and zincate (ZnO$_4$, blue) tetrahedra in bulk (left) and surface (right) sites of the FAU framework, superimposed with corresponding regular tetrahedrons (gray) determined by PolyDis package[30]. The length of each Al-O and Zn-O bond is displayed in color (in Å) and the length of bonds for each ideal tetrahedron is in black. Asterisks (*) indicate Brønsted-acidic oxygens. The geometry optimization is carried out using the "large" ONIOM partitioning scheme (see Figure S17).
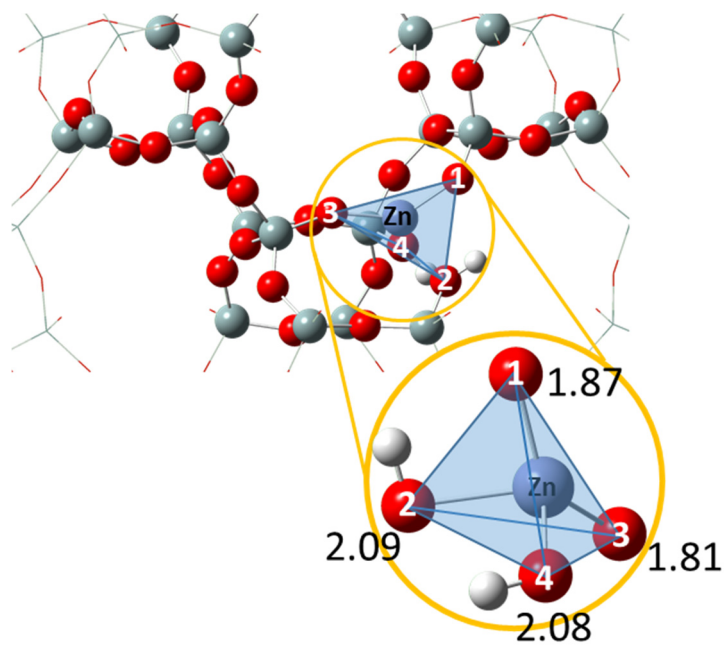
Figure S20. Optimized local geometry around Zn loaded into a bulk location of the GIS zeolite framework with Zn-O bond lengths (in Å). The geometry optimization is carried out using the "large" ONIOM partitioning scheme (see Figure S17).
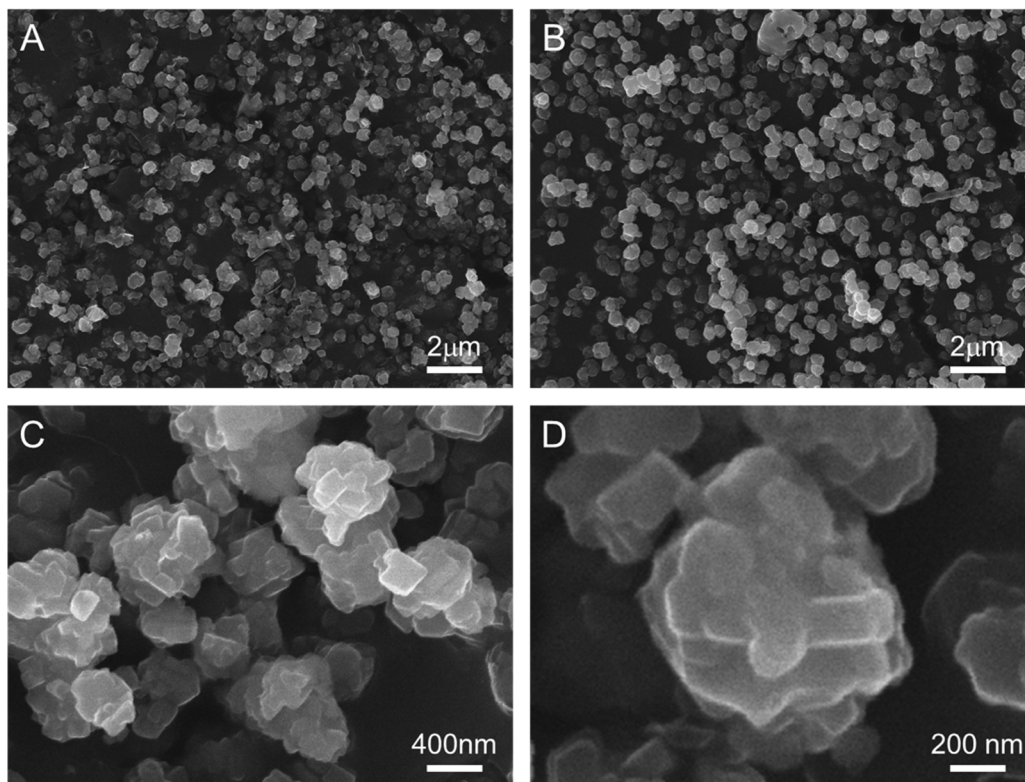
Figure S21. Scanning electron micrographs of Zn,Na-FAU crystals at various magnifications synthesized at 100°C for 3 days. All samples were prepared using a growth mixture with a molar composition of 9 SiO_2:0.5 Al_2O_3:0.32 Zn:11 NaOH:190 H_2O. Micrographs reveal the presence of putative intergrowths induced by the presence of Zn (see Figure 2a in the manuscript for FAU crystals synthesized using the same molar composition without Zn).
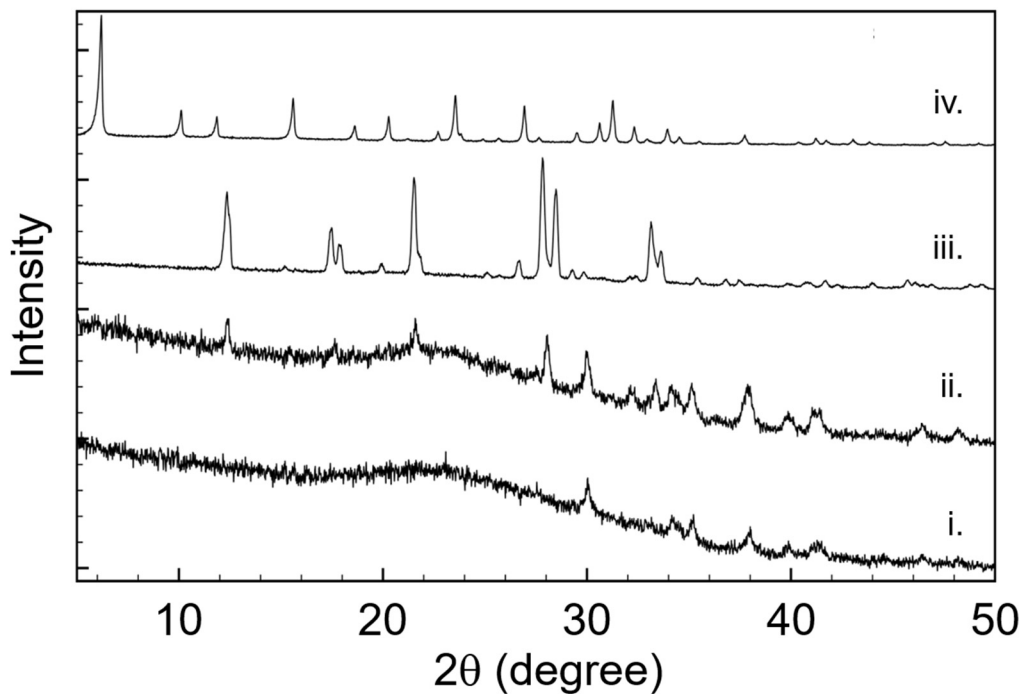
Figure S22. Powder XRD patterns for samples prepared from supernatant isolated from Na-FAU syntheses using a growth mixture with a molar composition of 9 SiO_2:0.5 Al_2O_3:11 NaOH:190 H_2O. Na-FAU was first prepared from hydrothermal treatment at 100°C for 6 h. Supernatant solution isolated from the latter was hydrothermally treated at 100°C for 2 h (i), 4 h (ii), and 16 h (iii) indicates the absence of a FAU intermediate during GIS – P2 crystallization (iii). A pure FAU powder XRD pattern is provided for reference (iv). Impurity peaks evident in profiles i and ii are artifacts of an incomplete washing protocol, which was used owing to the challenges of isolating crystal product from samples with little yield.
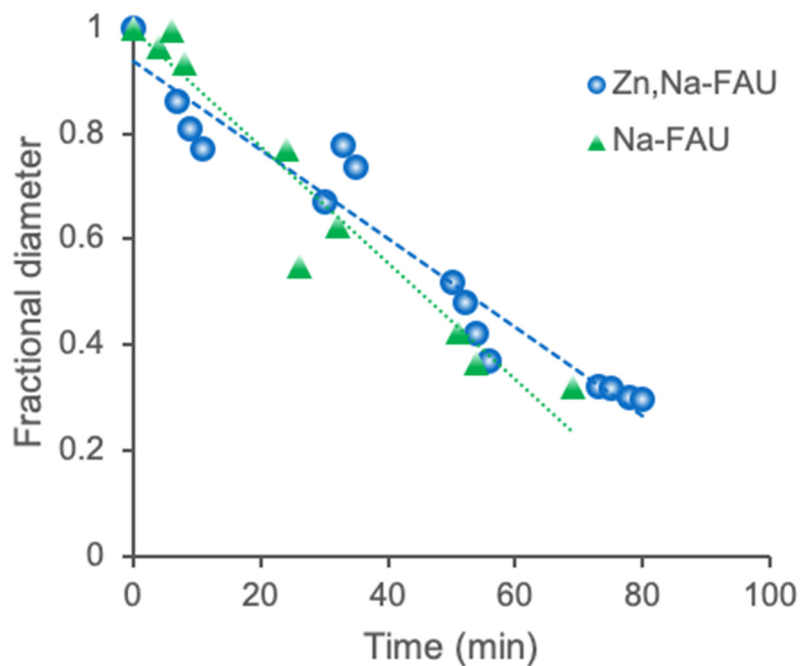
Figure S23. Dissolution of Zn,Na-FAU (blue circles) and Na-FAU (green triangles) in basic media, monitored using dynamic light scattering (DLS). Solid zeolite crystals were suspended (1 wt%) in DI water and sonicated for 5 min. The zeolite suspension and a solution of 0.25 M NaOH were separately placed in a water bath to reach the appropriate temperature (40°C). Then, the zeolite-containing solution was added to the NaOH solution (10 wt%) in the DLS sample vat. Each data point represents 2 min of collection time. CONTIN mathematical analysis was used to determine the particle size from the correlation function. Results reveal that dissolution profiles are qualitatively consistent regardless of whether Zn is present.
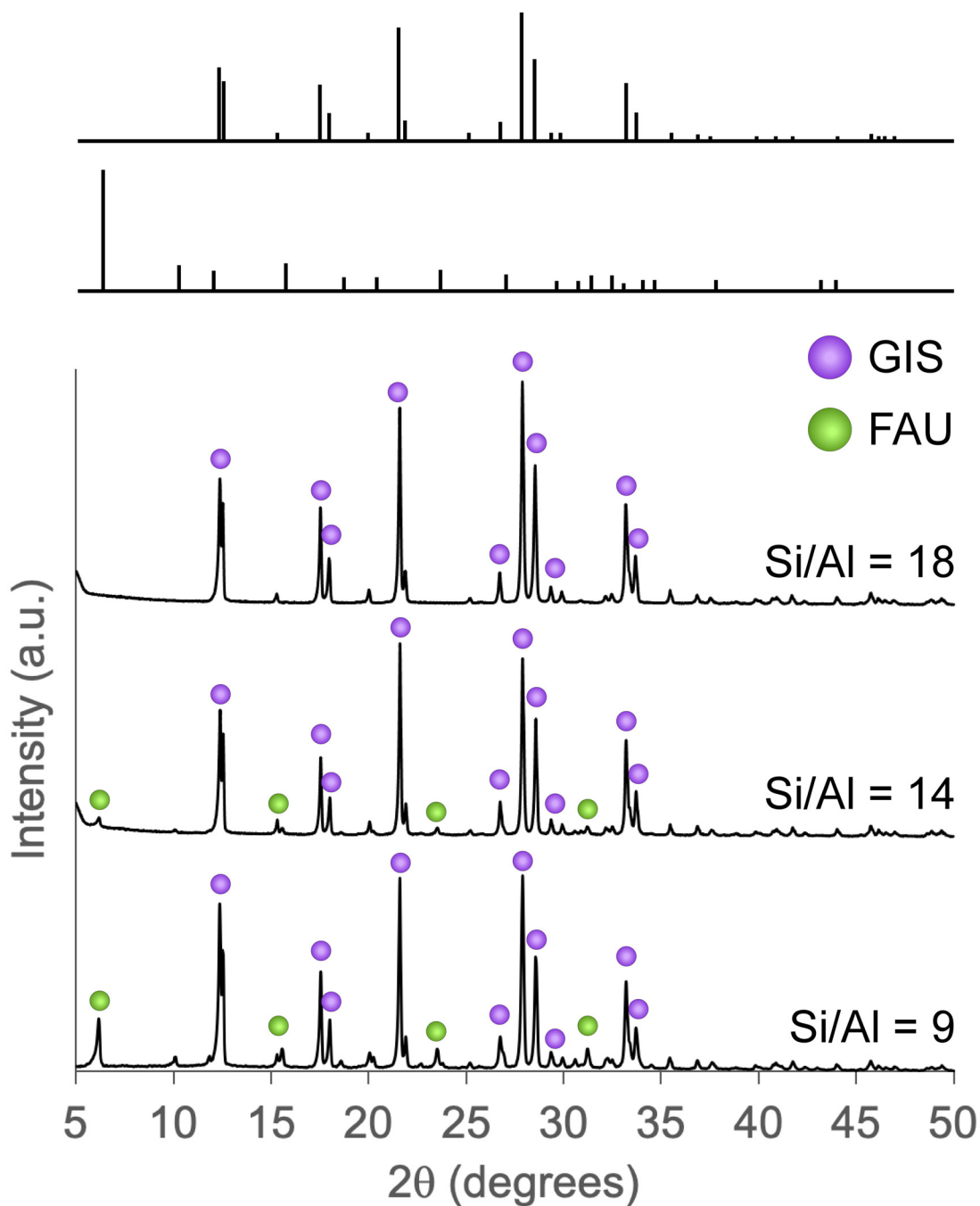
Figure S24. Powder XRD patterns for samples prepared from growth mixtures with a molar composition of 9 SiO_2:x Al_2O_3:11 NaOH:190 H_2O hydrothermally treated at 100°C for 3 days. The amount of aluminum (x) was varied to achieve the molar ratios indicated on the right side of each corresponding pattern. Select peaks are indicated using green (FAU) or purple (GIS – P2) circles. Reference patterns of GIS – P2 (top) and FAU (bottom) obtained from the International Zeolite Association Structure Database are displayed.
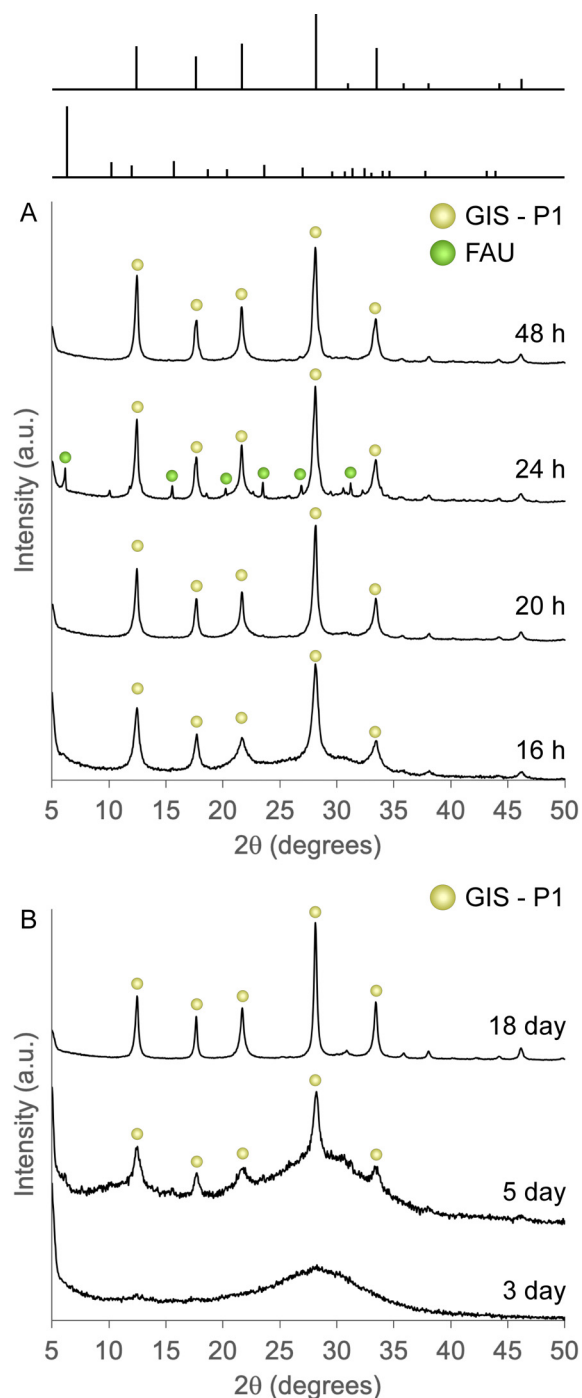
Figure S25. Powder XRD patterns for samples prepared using sodium silicate (rather than LUDOX AS-40) in growth mixtures with a molar composition of 9 SiO_2:0.5 Al_2O_3:x Zn:11 NaOH:190 H_2O. All samples were hydrothermally treated at 100°C. (A) In the absence of Zn ($x = 0$), GIS – P1 crystallizes initially with a FAU impurity phase forming after 24 h, prior to the crystallization of pure GIS – P1. (B) In the presence of Zn ($x = 0.35$), no FAU impurity is evident, but the crystallization of pure GIS – P1 takes significantly longer to achieve. Select peaks are indicated using green (FAU) or yellow (GIS – P1) circles. . Reference patterns of GIS – P1 (top) and FAU (bottom) obtained from the International Zeolite Association Structure Database are displayed.

Supporting Tables

Table S1. Shell-by-shell fits to Zn EXAFS spectra.

Sample	Zn/Al	Neighbor	CN	R + ΔR (Å)	σ^2	p(F)	ΔE_0	R Factor	Ref
Zn,Na-FAU-1	0.05	O	4*	1.945(6)	0.0029(4)	<0.001	4(1)	0.012	**
		Zn	1*	2.920(9)	0.003(1)	<0.001			
Zn,Na-FAU-2***	0.20	O	4.25*	1.94(1)	0.005(1)	<0.001	3(3)	0.082	**
		Al	1.37*	3.11(8)	0.009(11)	0.591			
Zn,Na-FAU-3***	0.22	O	4*	1.98(1)	0.0075(8)	<0.001	4(1)	0.025	6
		Zn	2*	3.32(2)	0.004(2)	0.071			
		Zn	2*	3.51(3)	0.005(3)	0.072			
Zn,Na-FAU-4	0.28	O	4*	1.943(4)	0.0041(3)	<0.001	5.8(6)	0.004	6
		Si	1*	3.15(2)	0.004(3)	0.033			
		Zn	2*	3.29(2)	0.012(3)	0.015			
Zn,Na-FAU-5	0.36	O	4*	1.947(5)	0.0045(4)	<0.001	6.1(8)	0.004	6
		Zn	2*	3.201(8)	0.003(2)	<0.001			
		Zn	2*	3.34(1)	0.003(2)	0.004			
Zn,Na-FAU-6	0.28	O	4*	1.947(6)	0.0045(5)	<0.001	6(1)	0.011	6
		Si	1*	3.14(2)	0.0005(30)	0.102			
		Zn	2*	3.30(4)	0.014(6)	0.117			
Zn,Na-FAU-7	0.27	O	5.40*	1.965(4)	0.0085(3)	<0.001	4.0(6)	0.005	6
		Zn	2.84*	3.33(2)	0.019(3)	0.008			
Zn,Na-FAU-8	0.37	O	5.25*	1.945(5)	0.0061(4)	<0.001	5.5(8)	0.006	6
		Si	1.12*	3.14(3)	0.004(5)	0.144			
		Zn	6(8)	3.31(3)	0.02(2)	0.079			
Precipitate from diluted supernatant	1	O	5.25*	1.951(6)	0.0059(4)	<0.001	5.9(9)	0.007	6
		Si	1.22*	3.12(3)	0.004(4)	0.197			
		Zn	11 (12)	3.33(3)	0.03(2)	0.058			
VPI-7	-	O	3*	1.948(7)	0.0050(5)	<0.001	7(1)	0.013	6
		Si	1*	3.19(5)	0.008(9)	0.189			
		Zn	2*	3.30(2)	0.010(3)	0.040			
FAU reference	-	O	4	1.858					
		Zn	1	2.848					
		Al	1	3.194					
Hemimorphite reference	-	O	4	1.948					
		Si	3	3.203					
		Zn	2	3.296					
		Zn	2	3.428					

S_o^2 = 0.8; coordination number (CN); k space fit window 2 – 11, Fourier transform fit window 1 – 3.25; interatomic distance (R + ΔR); disorder parameter (σ^2); energy shift (ΔE^0); goodness of fit parameter (R-factor); F-test [p(F)]. A F-test was performed on each scattering shell to determine the best model.[7] If the probability of F [p(F)] is less than 0.05, the addition of that shell improves the fit to greater than 2σ and that shell was considered to be observed in the experiments. *Fixed Value. ** Framework standard generated in VASP[7]. ***Zn,Na-FAU-2 and Zn,Na-FAU-3 were ion exchanged with Co^{2+} and NH_4^+, respectively.

Table S2. Experimental first-shell bond lengths of the FAU samples from PDF measurements.

Sample	Si/Al – O (Å)	Zn – O (Å)
Zn,Na-FAU (Zn/Al = 0.2)	1.60 ± 0.08*	1.95 ± 0.09*
Zn,Na-FAU (Zn/Al = 0.8)	1.63 ± 0.08*	1.95 ± 0.08*
FAU experimental	1.65 ± 0.09**	–
Hemimorphite reference[32]	1.621 ± 0.005	1.96 ± 0.02†

*Determined from D(r) profiles.
**Determined from G(r) profile.
†Error in all cases corresponds to 1σ standard deviation, equivalent to the width of the Gaussian fit to the data.

Table S3. Tetrahedral geometry upon Al or Zn substitution on FAU bulk and surface sites, determined from ONIOM calculations ("Large" partitioning scheme).

Substitution	Average T-O length (Å)	Average deviation* (%)
None	1.647 (0.006)**	1.7 (0.5)
Bulk Al	1.76 (0.08)	3.8 (1.1)
Surface Al	1.77 (0.07)	4.9 (1.3)
Bulk Zn	1.95 (0.12)	14 (6)
Surface Zn	1.97 (0.11)	16 (4)

*Deviation of positions of oxygen atoms relative to their corresponding positions in a regular tetrahedron, determined by PolyDis package[33].
**Numbers in parentheses refer to the standard deviation.

Table S4. Parametric analysis of growth mixtures using the products of synthesis mixtures as seeds in supernatant solutions and analogous samples prepared without seeds.

Seed	Supernatant[†]	Product	Si/Al[††]	Si/Zn[††]
Zn, Na-FAU*	Na-FAU	GIS	2.0	80
Na-FAU**	Zn, Na-FAU	FAU	2.3	14
None	Na-FAU	GIS	2.2	---
None	Zn, Na-FAU	Amorphous	---	---

[†]Supernatant was isolated from seed solutions using centrifuge
[††]Elemental compositions were obtained using electron dispersive spectroscopy (EDS)
*Zn,Na-FAU was obtained by hydrothermally treating a growth mixture of molar composition 9 SiO_2:0.5 Al_2O_3:0.35 Zn:11 NaOH:190 H_2O for 3 days at 100°C
**Na-FAU was obtained by hydrothermally treating a growth mixture of molar composition 9 SiO_2:0.5 Al_2O_3:11 NaOH:190 H_2O for 3 days at 80°C

References

(1) Anseau, M. R.; Leung, J. P.; Sahai, N.; Swaddle, T. W. Interactions of Silicate Ions with Zinc(II) and Aluminum(III) in Alkaline Aqueous Solution. *Inorganic Chemistry* **2005**, *44* (22), 8023-8032. DOI: 10.1021/ic050594c. McCormick, A. v.; Bell, A. T. The Solution Chemistry of Zeolite Precursors. *Catalysis Reviews* **1989**, *31* (1-2), 97-127. DOI: 10.1080/01614948909351349.

(2) Hoeher, A.; Mergelsberg, S.; Borkiewicz, O. J.; Dove, P. M.; Michel, F. M. A new method for in situ structural investigations of nano-sized amorphous and crystalline materials using mixed-flow reactors. *Acta Crystallographica Section A: Foundations and Advances* **2019**, *75* (5), 758-765.

(3) Toby, B. H.; Von Dreele, R. B. GSAS-II: the genesis of a modern open-source all purpose crystallography software package. *Journal of Applied Crystallography* **2013**, *46* (2), 544-549. DOI: 10.1107/s0021889813003531.

(4) Juhas, P.; Davis, T.; Farrow, C. L.; Billinge, S. J. L. PDFgetX3: a rapid and highly automatable program for processing powder diffraction data into total scattering pair distribution functions. *Journal of Applied Crystallography* **2013**, *46* (2), 560-566. DOI: 10.1107/s0021889813005190.

(5) Ravel, B.; Newville, M. ATHENA, ARTEMIS, HEPHAESTUS: data analysis for X-ray absorption spectroscopy using IFEFFIT. *Journal of Synchrotron Radiation* **2005**, *12* (4), 537-541.

(6) Libowitzky, E.; Kohler, T.; Armbruster, T.; Rossman, G. R. Proton disorder in dehydrated hemimorphite-IR spectroscopy and X-ray structure refinement at low and ambient temperatures. *European Journal of Mineralogy* **1997**, *9* (4), 803-810. DOI: 10.1127/ejm/9/4/0803.

(7) Downward, L.; Booth, C. H.; Lukens, W. W.; Bridges, F. A Variation of the F-Test for Determining Statistical Relevance of Particular Parameters in EXAFS Fits. In *13th International Conference on X-ray Absorption Fine Structure*, Stanford, CA, USA, 2006; American Institute of Physics (AIP): pp 129-131. DOI: 10.1021/ic102111t.

(8) Frisch, M. J.; Trucks, G. W.; Schlegel, H. B.; Scuseria, G. E.; Robb, M. A.; Cheeseman, J. R.; Scalmani, G.; Barone, V.; Mennucci, B.; Petersson, G. A. Gaussian 09, Revision D. 01, Gaussian, Inc., Wallingford CT. **2009**.

(9) Wang, Y.; Verma, P.; Jin, X.; Truhlar, D. G.; He, X. Revised M06 density functional for main-group and transition-metal chemistry. *Proceedings of the National Academy of Sciences* **2018**, *115* (41), 10257-10262.

(10) Barone, V.; Cossi, M. Quantum calculation of molecular energies and energy gradients in solution by a conductor solvent model. *The Journal of Physical Chemistry A* **1998**, *102* (11), 1995-2001.

(11) Trinh, T. T.; Jansen, A. P. J.; van Santen, R. A. Mechanism of oligomerization reactions of silica. *The Journal of Physical Chemistry B* **2006**, *110* (46), 23099-23106.

(12) Freeman, E. E.; Neeway, J. J.; Motkuri, R. K.; Rimer, J. D.; Mpourmpakis, G. Understanding initial zeolite oligomerization steps with first principles calculations. *AIChE Journal* **2020**, *66* (12), e17107.

(13) Svensson, M.; Humbel, S.; Froese, R. D. J.; Matsubara, T.; Sieber, S.; Morokuma, K. ONIOM: a multilayered integrated MO+MM method for geometry optimizations and single point energy predictions. A test for Diels− Alder reactions and Pt $(P(t-Bu)_3)^{2+}$ H_2 oxidative addition. *The Journal of Physical Chemistry* **1996**, *100* (50), 19357-19363. Humbel, S.; Sieber, S.; Morokuma, K. The IMOMO method: Integration of different levels of molecular orbital approximations for geometry optimization of large systems: Test for nbutane conformation and SN-2 reaction: $RCl+Cl^-$. *The Journal of Chemical Physics* **1996**, *105* (5), 1959-1967. Dapprich, S.; Komáromi, I.; Byun, K. S.; Morokuma, K.; Frisch, M. J. A new ONIOM implementation in Gaussian98. Part I. The calculation of energies, gradients, vibrational frequencies and electric field derivatives. *Journal of Molecular Structure: THEOCHEM* **1999**, *461*, 1-21. Vreven, T.; Morokuma, K. On the application of the IMOMO (integrated molecular orbital+ molecular orbital) method. *Journal of Computational Chemistry* **2000**, *21* (16), 1419-1432.

(14) Atoguchi, T.; Yao, S. Ti atom in MFI zeolite framework: a large cluster model study by ONIOM method. *Journal of Molecular Catalysis A: Chemical* **2003**, *191* (2), 281-288. Montejo-Valencia, B. D.; Pagán-Torres, Y. J.; Martínez-Iñesta, M. M.; Curet-Arana, M. C. Density functional theory (DFT) study to unravel the catalytic properties of M-exchanged MFI, (M= Be, Co, Cu, Mg, Mn, Zn) for the conversion of methane and carbon dioxide to acetic acid. *ACS Catalysis* **2017**, *7* (10), 6719-6728.

(15) Kostetskyy, P.; Mpourmpakis, G. Computational insights into adsorption of C4 hydrocarbons in cation-exchanged ZSM-12 zeolites. *Industrial & Engineering Chemistry Research* **2017**, *56* (24), 7062-7069.

(16) Stewart, J. J. P. Optimization of parameters for semiempirical methods V: Modification of NDDO approximations and application to 70 elements. *Journal of Molecular Modeling* **2007**, *13* (12), 1173-1213.

(17) Evans, M. G.; Polanyi, M. Further considerations on the thermodynamics of chemical equilibria and reaction rates. *Transactions of the Faraday Society* **1936**, *32*, 1333-1360.

(18) Gasteiger, H. A.; Frederick, W. J.; Streisel, R. C. Solubility of aluminosilicates in alkaline solutions and a thermodynamic equilibrium model. *Industrial & Engineering Chemistry Research* **1992**, *31* (4), 1183-1190.

(19) Barrer, R. M. Zeolites and their synthesis. *Zeolites* **1981**, *1* (3), 130-140.

(20) Domine, D.; Quobex, J. Synthesis of mordenite. *Molecular sieves. Society of Chemical Industry, London* **1968**, *78*. Meise, W.; Schwochow, F. Kinetic studies on the formation of zeolite A. ACS Publications, 1973.

(21) Mora-Fonz, M. J.; Catlow, C. R. A.; Lewis, D. W. Oligomerization and cyclization processes in the nucleation of microporous silicas. *Angewandte Chemie* **2005**, *117* (20), 3142-3146. Mora-Fonz, M.; Hamad, S.; Catlow, C. Modelling nucleation and nano-particle structures. *Molecular Physics* **2007**, *105* (2-3), 177-187.

(22) White, C. E.; Provis, J. L.; Kearley, G. J.; Riley, D. P.; Van Deventer, J. S. Density functional modelling of silicate and aluminosilicate dimerisation solution chemistry. *Dalton Transactions* **2011**, *40* (6), 1348-1355.

(23) Klamt, A.; Schüürmann, G. COSMO: a new approach to dielectric screening in solvents with explicit expressions for the screening energy and its gradient. *Journal of the Chemical Society, Perkin Transactions 2* **1993**, (5), 799-805.

(24) Trinh, T. T.; Jansen, A. P.; van Santen, R. A. Mechanism of oligomerization reactions of silica. *The Journal of Physical Chemistry B* **2006**, *110* (46), 23099-23106.

(25) McIntosh, G. J. A theoretical kinetic model of the temperature and pH dependent dimerization of orthosilicic acid in aqueous solution. *Physical Chemistry Chemical Physics* **2012**, *14* (2), 996-1013. Greenberg, S. A.; Sinclair, D. The polymerization of silicic acid. *The Journal of Physical Chemistry* **1955**, *59* (5), 435-440. Zhang, X.-Q.; Trinh, T. T.; van Santen, R. A.; Jansen, A. P. Mechanism of the initial stage of silicate oligomerization. *Journal of the American Chemical Society* **2011**, *133* (17), 6613-6625.

(26) Namuangruk, S.; Pantu, P.; Limtrakul, J. Alkylation of benzene with ethylene over faujasite zeolite investigated by the ONIOM method. *Journal of Catalysis* **2004**, *225* (2), 523-530. Shiota, Y.; Suzuki, K.; Yoshizawa, K. QM/MM study on the catalytic mechanism of benzene hydroxylation over Fe−ZSM-5. *Organometallics* **2006**, *25* (13), 3118-3123.

(27) Gomes, J.; Zimmerman, P. M.; Head-Gordon, M.; Bell, A. T. Accurate prediction of hydrocarbon interactions with zeolites utilizing improved exchange-correlation functionals and QM/MM methods: benchmark calculations of adsorption enthalpies and application to ethene methylation by methanol. *The Journal of Physical Chemistry C* **2012**, *116* (29), 15406-15414.

(28) Li, Y.; Guo, W.; Yuan, S.; Fan, W.; Wang, J.; Jiao, H. Effective ONIOM schemes for modeling MCM-22 zeolite. *Journal of Molecular Structure: THEOCHEM* **2009**, *916* (1-3), 53-60.

(29) Montejo-Valencia, B. D.; Salcedo-Pérez, J. L.; Curet-Arana, M. C. DFT study of closed and open sites of BEA, FAU, MFI, and BEC zeolites substituted with tin and titanium. *The Journal of Physical Chemistry C* **2016**, *120* (4), 2176-2186.

(30) Stoiber, D.; Niewa, R. PolyDis: simple quantification tool for distortion of polyhedra in crystalline solids. *Zeitschrift für Kristallographie-Crystalline Materials* **2019**, *234* (3), 201-209.

(31) Zuo, Q.; Yang, J.; Shi, Y.; Wu, D. Activating hemimorphite using a sulfidation-flotation process with sodium sulfosalicylate as the complexing agent. *Journal of Materials Research and Technology* **2020**, *9* (5), 10110-10120.

(32) Takeuchi, Y.; Sasaki, S.; Joswig, W.; Fuess, H. X-ray and neutron diffraction study of hemimorphite. *Proceedings of the Japan Academy, Series B* **1978**, *54* (10), 577-582.

(33) Stoiber, D.; Niewa, R. PolyDis: simple quantification tool for distortion of polyhedra in crystalline solids. *Zeitschrift für Kristallographie - Crystalline Materials* **2019**, *234* (3), 201-209.